Universitetet
i Stavanger

Faculty of Science and Technology

MASTER'S THESIS

Study program/Specialization: Petroleum Geosciences Engineering	Spring, 2014 Open
Writer: Xiaoan Zhong	 _____ (Writer's signature)
Faculty supervisor: R. James Brown External supervisor(s): Børge Rosland	
Title of thesis: Low-frequency reflection seismic and direct hydrocarbon indication	
Credits (ECTS): 30	
Keywords: Low frequency Amplitude attenuation Hydrocarbon indication Reflection seismic Spectral decomposition Instantaneous spectral analysis	Pages: 65 Stavanger, 15th June, 2014

Low-frequency reflection seismic and direct hydrocarbon indication

by

Xiaoan Zhong, B.Sc.

Thesis

Presented to the Faculty of Science and Technology

The University of Stavanger

The University of Stavanger

June 2014

Acknowledgements

Abstract

Low-frequency reflection seismic and direct hydrocarbon indication

Xiaoan Zhong, M.Sc.

The University of Stavanger, 2014

Supervisors: R. James Brown; Børge Rosland

Low-frequency reflection seismic has been used as an indicator to detect hydrocarbons in petroliferous reservoirs. A number of spectral decomposition methods have been developed to derive seismic from time to frequency domain. The application of low-frequency seismic computed by the Gabor-Morlet transform (GMT) and instantaneous spectral analysis (ISA) methods revealed one of low-frequency shadow effects, amplitude attenuation, in the southern North Sea. According to computed low-frequency (< 20 Hz) instantaneous spectral profiles through discovered wells, strong responses are observed on hydrocarbon-saturated intervals. By contrast, on higher frequency (> 20 Hz) instantaneous spectral profiles, frequency amplitude is vanished from the petroliferous intervals, however, strong responses are presented either above or below these pay zones. The loss mechanism of high-frequency energy is considered to be contributed by P-wave attenuation of stratigraphic heterogeneity. This type of low-frequency shadow effect can illustrate the probable existence of an oil reservoir and can be applied to detect the existence of hydrocarbon directly. Based on the distribution of attenuated frequency amplitude, a total of 140 km^2 of prospects have been identified from both Cretaceous-Paleogene chalk reservoirs and sandstones beneath the basal Cretaceous unconformity (BCU).

The identified chalk prospects are mainly distributed along the rim of anticlines on the Lindesnes Ridge, while prospective clastics are stratigraphically entrapped on the slope of the Grensen Nose. In addition to using low-frequency reflection seismic to detect hydrocarbon directly, frequency components can be applied to calibrate the interpretations of horizons and faults as well.

Table of Contents

List of Figures

List of Tables

1 Introduction

As a significant part of reflected seismic waves, anomalous frequencies less than 20 Hz appear to have been first observed to be associated with hydrocarbon reservoirs by Taner et al. (1979). Since then, a number of laboratory and field examples have been reported in the literature where the low-frequency components of reflected seismic waves have been used as hydrocarbon indicators to image, delineate, and monitor petroliferous reservoirs (Taylor et al., 2000; Cai et al., 2008; Wang et al., 2009; Liu et al., 2010; Pu, 2011; Long et al., 2012; Yang et al., 2012). These indicators include low-frequency shadow with hydrocarbon deposits, low-frequency energy anomalies, and instantaneous wavelet energy absorption analysis, etc. (Chen et al., 2012).

In reflection-seismic field data acquired for petroleum exploration and/or production, low-frequency shadow effects, such as time delay, phase distortion, frequency decrease, and amplitude attenuation, have been observed and provided evidences of hydrocarbon existence (Goloshubin et al., 2002; Castagna et al., 2003; Sinha et al., 2005; Odebeatu et al., 2006; Huang et al., 2007; Kazemeini et al., 2009; Silin et al., 2010; Yu et al., 2011; Zhang et al., 2012; Chen et al., 2013).

For example, Chen et al. (2012) computed a series of instantaneous spectral sections from stacked seismic data (Figure 1a), and illustrated amplitude attenuation effect by comparing produced spectral profiles. On the 12 Hz section (Figure 1b), the bright gas reservoir (indicated by a black arrow) and strong low-frequency shadow (outlined by a black contour) lie immediately underneath the reservoir. On the 36 Hz section (Figure 1c), the gas reservoir still remains bright, whereas the low-frequency shadow has disappeared.
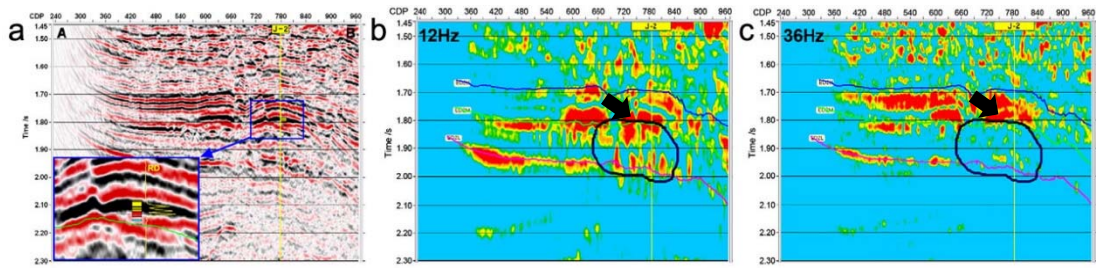
Figure 1. Instantaneous spectral sections corresponding to the stacked seismic profile

To derive frequency components from reflection seismic, spectral decomposition has been regarded as an effective technology. As summarized by Castagna et al. (2003), three steps are involved for spectral decomposition: (1) utilize wavelet transform methods to decompose the seismogram into constituent wavelets; (2) produce "frequency gathers" by summing up the transformed spectra (e.g. Fourier spectra) of the individual wavelets in the time-frequency domain; and (3) sort the frequency gathers to produce common frequency cubes, sections, time slices, and horizon slices, etc.

There are a variety of spectral decomposition methods, which include the discrete Fourier transform (DFT), the short-time Fourier transform (STFT), enhanced spectral processing (ESP), the maximum entropy method (MEM), the continuous wavelet transform (CWT), matching pursuit decomposition (MPD), the Gabor-Morlet transform (GMT), and instantaneous spectral analysis (ISA), etc.

Qian et al. (1994) and Partyka et al. (1999) applied the discrete Fourier transform (DFT) to generate discrete-frequency energy cubes for reservoir characterization. However, vertical resolution of the DFT is limited due to frequency localization loss when the seismogram is windowed (Castagna et al., 2003; Sinha et al., 2005).

The short-time Fourier transform (STFT) extracts the frequency content of the signal and produces a 2D representative profile of frequencies versus time by adding a small time-domain window and shifting this window appropriately (Okaya et al.,

2

1992). The vertical resolution is fixed over the entire time-frequency plane when a window function has been chosen for an STFT.

Enhanced spectral processing (ESP) eliminated the windowing problem in the above Fourier spectral analysis (Sun et al., 2002).

The continuous wavelet transform (CWT) decomposes a function by band-pass filtering the original signal at different band-widths. In practice, the CWT has higher frequency resolution for low frequencies and better time resolution for higher frequencies (Chakraborty et al., 1995). As an extensional version of CWT, Stockwell et al. (1996) introduced an S-transform algorithm based on a moving and scalable localizing Gaussian window. Differentiating itself from other methods, S-Transform is an invertible transform which is closely related to the Fourier transform.

Mallat et al. (1993) introduced the matching-pursuit decomposition (MPD) to detect low-frequency shadows beneath hydrocarbon reservoirs. Because of excellent localization behavior of the MPD, reflections can be enhanced and surface waves and other types of noise can be eliminated using polygonal filters (Chakraborty et al., 1995; Huang et al., 2007).

Castagna et al. (2003) presented a method known as instantaneous spectral analysis (ISA).The ISA method selects the wavelet dictionary to better capture the features of the seismogram while selecting parameters judiciously and avoiding as many cross-correlation operations as possible to achieve reasonable computation time. Testified by various field examples, spectral decomposition with ISA has been done accurately with acceptable speed while simultaneously achieving excellent time and frequency resolution. As one of their examples, low-frequency shadow beneath the gas-filled sandstone reservoirs (red filled on stacked seismic) shows strongest event on the 10 Hz common-frequency section (Figure 2a), then it persists but is weaker than the overlying gas sands on the 20 Hz common-frequency section (Figure 2b), and finally it has disappeared on the 30 Hz common-frequency section (Figure 2c).
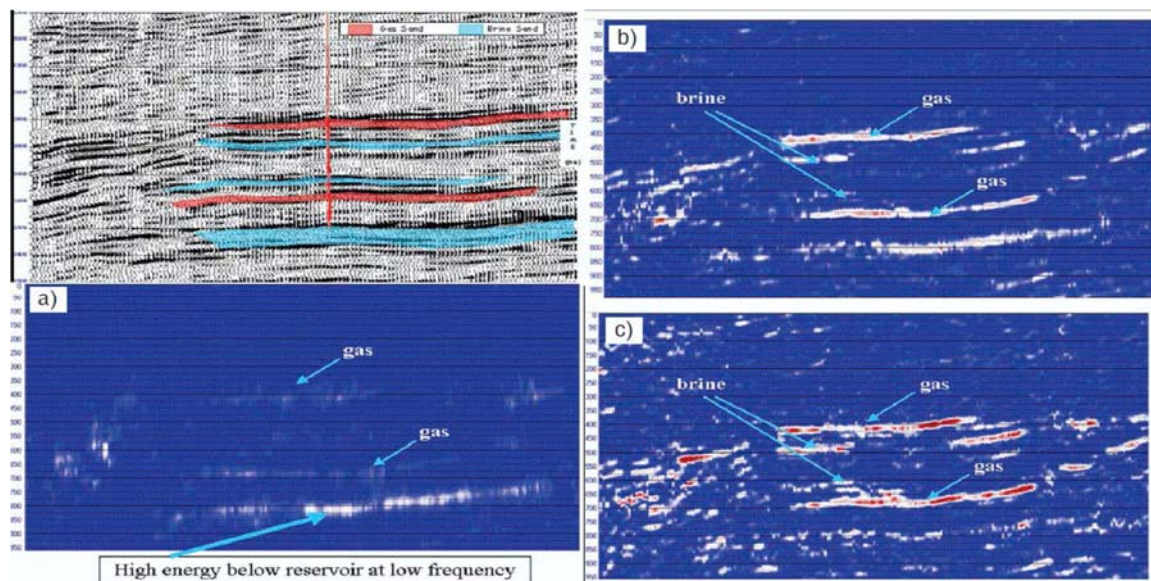
Figure 2. ISA sections corresponding to the stacked seismic profile

The Gabor-Morlet transform (GMT) filters the seismic data with a series of Gabor-Morlet wavelets to obtain narrow-band analytic traces. Divided by the original trace envelope, narrow-band traces are normalized to remove the amplitude variation of individual reflected events (Morlet et al., 1982, Taner 1983, Qian et al., 1999).

All spectral decomposition methods have their own advantages and disadvantages, different methods are required regarding to different applications (Castagna et al., 2006; Pang et al., 2013).

In this project, the ISA method is applied to generate frequency spectra along specific seismic lines, and the computed frequency spectra range from 2 to 15 Hz at steps of 1 Hz. The purpose of creating ISA volumes is to match frequency responses with fluid content which was reported by penetrated wells.

In the Rock Solid Attribute module of IHS Kingdom software, the GMT method is applied to produce time-frequency envelopes of user-defined frequency bands. Frequency attribute analysis is performed on these envelopes to identify low-frequency shadow effects.

4

2 Geological background

The study area is located in the Western Graben of the southern North Sea, approximately 260 km southwest of the Farsund coast, Norway, and it is adjacent to the United Kingdom and Denmark sectors (Figure 3). As a proved petroliferous province, several oil and gas fields have been discovered on Lindesnes Ridge, e.g. Eldfisk, Embla, Valhall, and Hod, etc. (Figure 4). This research is focused on the depression between the Grensen Nose and the Lindesnes Ridge, which is bounded by several prominent NW-SE normal faults (Zanella et al., 2003; Gennaro et al., 2013).

Figure 3. Location map of study area in the southern North Sea

(Tectonic framework after Brekke, 2000; location map after Gennaro et al., 2013)

Age (Ma)	Chronostratigraphy			Lithostratigraphy	Tectonic events	Hydrocarbon fields & wells

Age (Ma) / Chronostratigraphy

- 2.6 — Quaternary
- Tertiary — Neogene — Pliocene
- Tertiary — Neogene — Miocene
- Tertiary — Paleogene — Oligocene
- Tertiary — Paleogene — Eocene
- 66 — Tertiary — Paleogene — Paleocene
- Cretaceous — Upper — Maastrichtian, Campanian, Santonian, Coniacian, Turonian, Cenomanian
- Cretaceous — Lower — Albian, Aptian, Barremian, Hauterivian, Valanginian, Berriasian
- 145 — Jurassic — Upper — Tithonian, Kimmeridgian, Oxfordian
- Jurassic — Middle — Callovian, Bathonian, Bajocian, Aalenian
- Jurassic — Lower — Toarcian, Pliensbachian, Sinemurian, Hettangian
- 201 — Triassic — Upper — Rhaetian, Norian, Carnian
- Triassic — Middle — Ladinian, Anisian
- Triassic — Lower — Olenekian, Induan
- 252 — Permian — Lopingian
- Permian — Guadalupian
- 299 — Permian — Cisuralian
- Carboniferous — Pennsylvanian
- Carboniferous — Mississippian
- 359 — Devonian — Upper — Famennian, Frasnian
- Devonian — Middle — Givetian, Eifelian
- Devonian — Lower — Emsian, Pragian, Lochkovian
- 419

Lithostratigraphy

- NORDLAND GROUP
- HORDALAND GROUP
- BALDER FM
- EKOFISK FM
- TOR FM
- HOD FM
- HIDRA FM
- CROMER KNOLL
- ULA FM / MANDAL FM / ULA FM
- FARSUND FM
- BRYNE FM
- SMITH BANK FM
- ZECHSTEIN
- ROTLIEGENDES

Tectonic events

- Localized inversion
- Onset of sea-floor spreading and renewed rifting
- Fourth episode of rifting and onset of sea-floor spreading
- End Jurassic compression
- Third episode of rifting
- North Sea dome uplift & erosion
- Second episode of rifting
- First episode of rifting ?
- Sag phase ?

Hydrocarbon fields & wells

- Hod 2/11-2
- Embla
- 2/7-2
- Hod
- 2/7-31
- 2/7-29
- 2/7-19
- 2/10-1S
- 2/7-31
- Embla 2/7-22

Notes:

[1] Numerical ages, systems, and series are referenced from International Chronostratigraphic Chart v2013/01. International Commission on Stratigraphy.

[2] Lithostratigrapgy chart after Permian is modified from Deegan et al. (1977), Rossland et al. (2013), and Brasher et al. (1996).

[3] Lithostratigrapgic chart of Carboniferous is modified from Casey et al. (1993).

[4] Lithostratigrapgy chart of Devonian is modified from Lee et al. (1993).

[5] Tectonic events are summarized after Blystad et al. (1995), & Zanella et al. (2003).

[6] Hydrocarbon fields and wells are based on Factpages of Norwegian Petroleum Directorate public database.

Legends

- Oil
- Oil shows
- Gas shows
- Silty claystone
- Sandtone
- Conglomerate
- Carbonate
- Evaporite
- Coal

Figure 4. Stratigraphic chart of southern North Sea

(References of the chart are listed on the right-hand side of the column)

2.1 Tectonic events

According to Müller et al. (1992), Brekke (2000), Mosar (2003), Zanella et al. (2003), Wilson et al. (2006), Gołedowski et al.(2012), and Rossland et al. (2013), the southern North Sea underwent eight stages of tectonic events: (1) sag phase during Devonian; (2) first extension and rifting episode from Carboniferous to Permian; (3) second extension and rifting episode during Triassic; (4) North Sea dome rift and erosion in early Jurassic; (5) third extension and rifting episode during m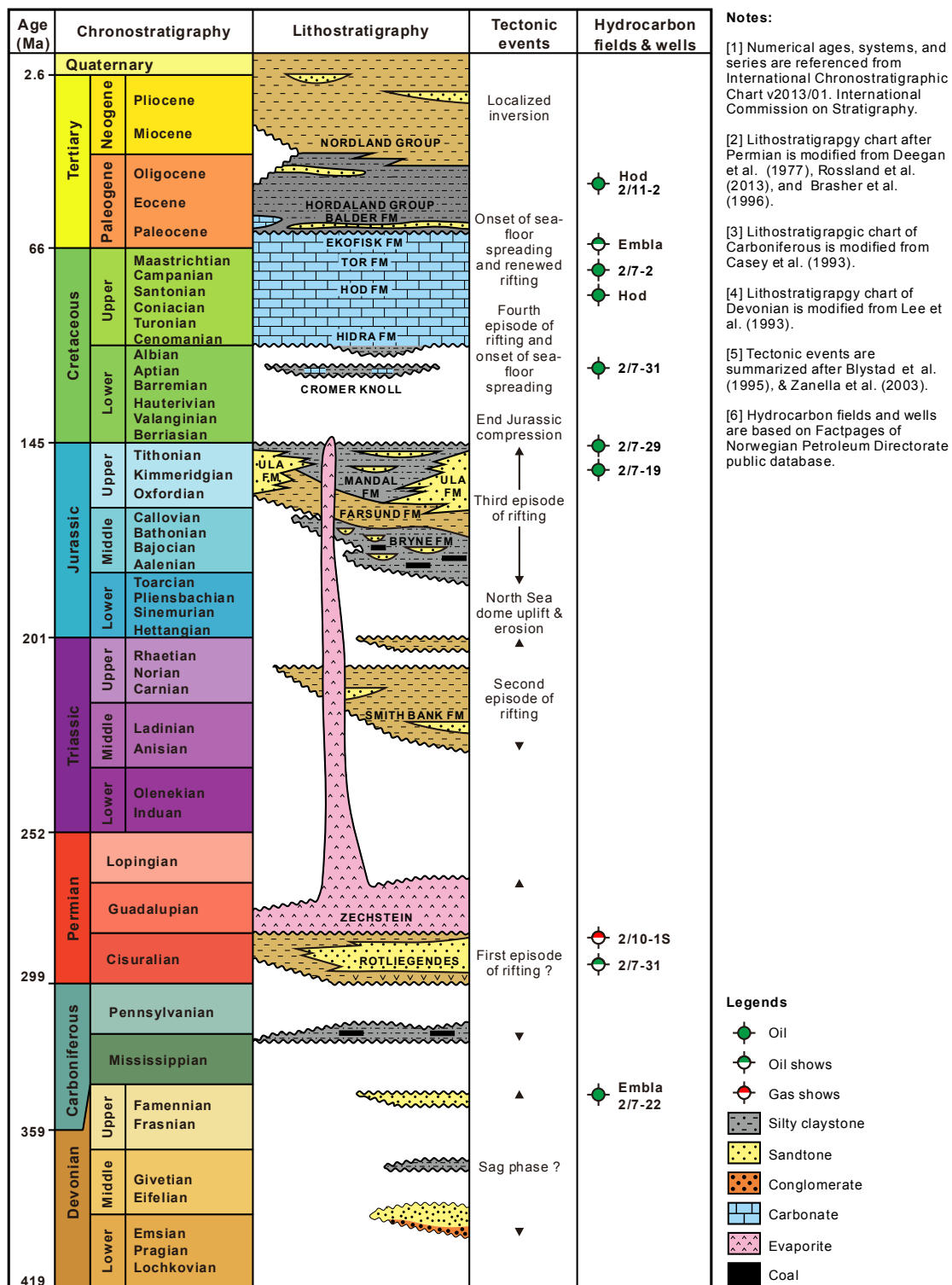iddle to late Jurassic; (6) end Jurassic compression; (7) fourth rifting episode and onset of sea-floor spreading during early Cretaceous; (8) onset of sea-floor spreading and renewed rifting from late Cretaceous to early Paleogene; and (9) localized inversion in Neogene (Figure 4).

There is a significant tectonic and sedimentary break between Late Jurassic and Early Cretaceous. The contact surface of the strata is featured by a widely distributed unconformity throughout the North Sea, which is called "basal Cretaceous unconformity" or "BCU" for abbreviation (Rawson et al., 1982; Blystad et al., 1995).

2.2 Petroleum systems and entrapment

Discovered fields have proved a working petroleum system in southern North Sea, especially on the Lindesnes Ridge. Based on trapping mechanism, there are two types of entrapment: (1) Pre-Cretaceous structural and stratigraphic trap with dip and fault closure laterally and overburden shale sealing vertically, e.g. Embla Field, the 2/7-19 discovery, and the 2/7-31 discovery, etc. (Marshall et al., 2003; NPD, 2014); and (2) Late Cretaceous to Paleocene fractured anticline overlying steeply dipping salt structures, e.g. Eldfisk Field, Valhall Field, Hod Field, etc. (Surlyk et al., 2003; NPD, 2014).

2.2.1 Embla Field

Located on the western flank of Lindesnes Ridge, the Embla field was discovered in 1974 by the 2/7-9 well, and it has Pre-Jurassic structural and stratigraphic trapping with dip and fault closure laterally and Jurassic shale sealing vertically (Marshall et al., 2003). Reservoir rocks comprise over 400 m of braided fluvial and alluvial fan sandstones from Devonian to Permian, and are interbeded by a complex floodplain/lacustrine mudstone, volcanic, and intrusive unit (Knight et al., 1993; Munz et al., 1998).

Ohm et al. (2012) performed geochemistry analysis and suggested that oil of Paleozoic age charged the field at the end of the Triassic. The Paleozoic oil was biodegraded at the oil-water contact during the Jurassic uplift and erosion, which caused poor production on the flank. Meanwhile, hydrocarbons in the crest of the structure escaped due to erosion of the seal. Subsidence occurred during the Cretaceous and formed a new seal and the Upper Jurassic oil reached a mature window and charged the structure along its carrier system.

2.2.2 Eldfisk Field

Located in the northern part of Lindesnes Ridge, the Eldfisk field was discovered in 1970 with the 2/7-1X well, and is one of the largest chalk fields with four-way closure (Herrington et al., 1991). Salt diapirism from the Upper Permian Zechstein Group penetrated through the overlying beds and generated significant anticlines in shallower formations (Jenyon 1985). The Eldfisk structure comprises three domes which were induced by salt flowage (Figure 5).

The Eldfisk reservoirs are composed of chalks of the Paleocene Ekofisk Formation, and the Late Cretaceous Hod and Tor Formations (Brasher et al., 1996).

In the Eldfisk field, hydrocarbons were generated from Upper Jurassic Kimmeridgian shale charged into chalk reservoirs and then effectively sealed by fine-grained Paleogene mudstone (Gautier 2005).
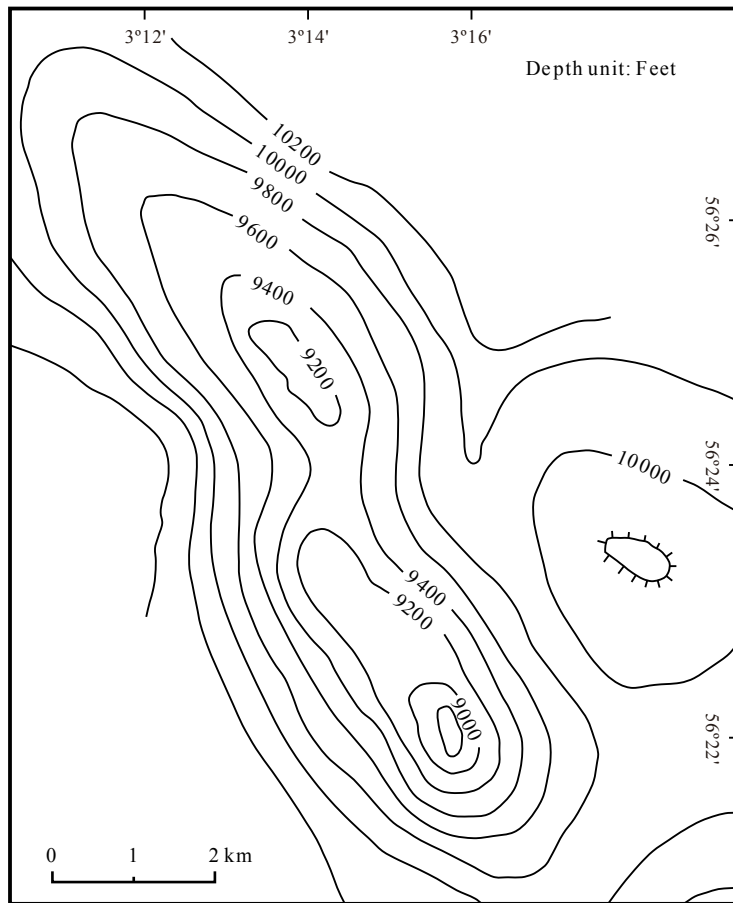
Figure 5. Top Eldfisk field structural map

(Modified after Maliva et al., 1992)

3 Database

From this chapter on, all figures and tables were produced by the author.

3.1 Seismic data

The research area is covered by a 1585 km^2 of 3D reflection seismic survey acquired in 2012. This is a modern broadband data set with record length of 7680 ms. The acquisition sampling rate was 2 ms and the processing was performed at 4 ms sampling. However, seismic volumes of dataset are limited within a 554 km^2 coverage (Figure 6).
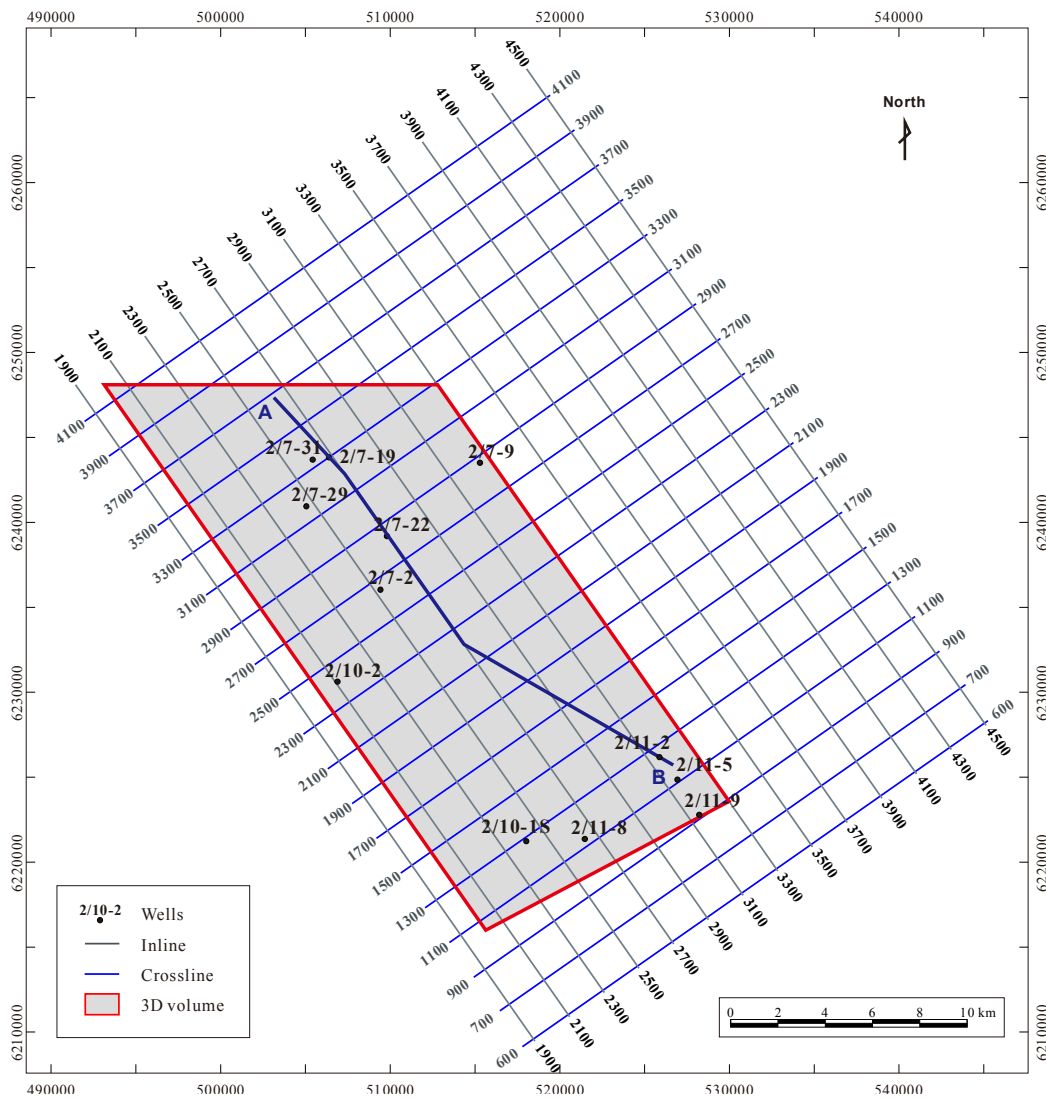

Figure 6. 3D reflection seismic coverage map

Available seismic volumes consist of the following groups: (1) a post-stack time migration (PSTM) gather under positive polarity; (2) full-volume time-frequency envelopes of 4.8, 7.2, 9.4, 12, 15.5, 20, 30, 40, and 50 Hz common frequencies; and (3) 2 to 15 Hz ISA cubes crossing key wells at steps of 1 Hz (Table 1).

Table 1. ISA volume list through key wells

No.	Well	Direction	
		Inline	Crossline
1	2/7-2	2522	
2	2/7-9	3208	
3	2/7-19	2688	3306
4	2/7-22	2700	
5	2/7-29	2466	3176
6	2/7-31	2618	
7	2/10-1S	2410	
8	2/10-2	2112	
9	2/11-2	3190	
10	2/11-5	3156	
11	2/11-8	2648	
12	2/11-9	3144	

A tuning-thickness analysis was performed to determine the vertical resolution for this survey, the author suggests that the minimum resolvable time-thickness of a bed is 9 ms (Figure 7a).
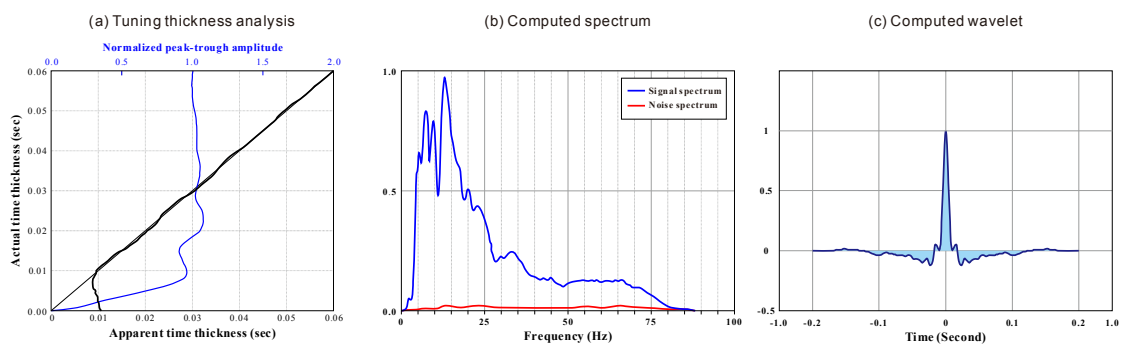

Figure 7. PSTM gather computation

(a) Tuning thickness analysis; (b) computed spectrum; (c) computed wavelet.
(Computations are done by the author)

11

In addition, the computed spectrum of PSTM gathers (Figure 7b) indicates that the frequency of seismic volume has higher concentration between 5 and 20 Hz, which is thought to be favorable frequency band for determining fluid mobility.

Moreover, a zero-phase wavelet for the PSTM gather was computed for further synthetics processing (Figure 7c).

Nevertheless, due to the influence of gas in reservoirs, 3D seismic data from the Lindesnes Ridge is obscure and of poor quality. As a solution, more than 1600 km of 2D seismic data were interpreted to demonstrate the structures along key horizons in the Western Graben.

3.2 Hydrocarbon discoveries from NPD wells

In the area of interest, 12 exploration wells have been penetrated since 1970, most of which were reported with hydrocarbons (NPD, 2014). Well data was extracted and summarized from the shared database of the Norwegian Petroleum Directorate (NPD).

3.2.1 Hydrocarbon beneath BCU

Oil and gas were proved beneath BCU during drill stem tests (DST) or core analysis from the 2/7-9, 2/7-19, 2/7-22, 2/7-29, and 2/7-31 wells. Fluids from these wells show that hydrocarbon was found surrounding the rim of the northern sub-sag of the Western Graben source kitchen (Figure 8).

(1) 2/7-9 well

The Embla field was found due to discoveries in the 2/7-9 well, and its reservoirs comprise sands from Devonian to Permian. A 111-m net pay zone with average porosity of 13 % and oil saturation of 55 % was encountered in the Late Jurassic sands. One DST was performed in the Devonian sandstones at 4313-4356 m, showing that 36 sm^3 (standard cubic meters) oil and 10 000 sm^3 gas per day was produced through a 32/64" choke after acidation.

(2) 2/7-19 well

Gas-bearing sands were encountered in the Upper Jurassic Ula Formation, and hydrocarbon was proved in the re-entry DST due to a blow-out preventer (BOP) system problem in the original well. Acid-treated Upper Jurassic sands produced 34.8 sm^3 oil and 15 631 sm^3 gas per day through an 11.91 mm choke.
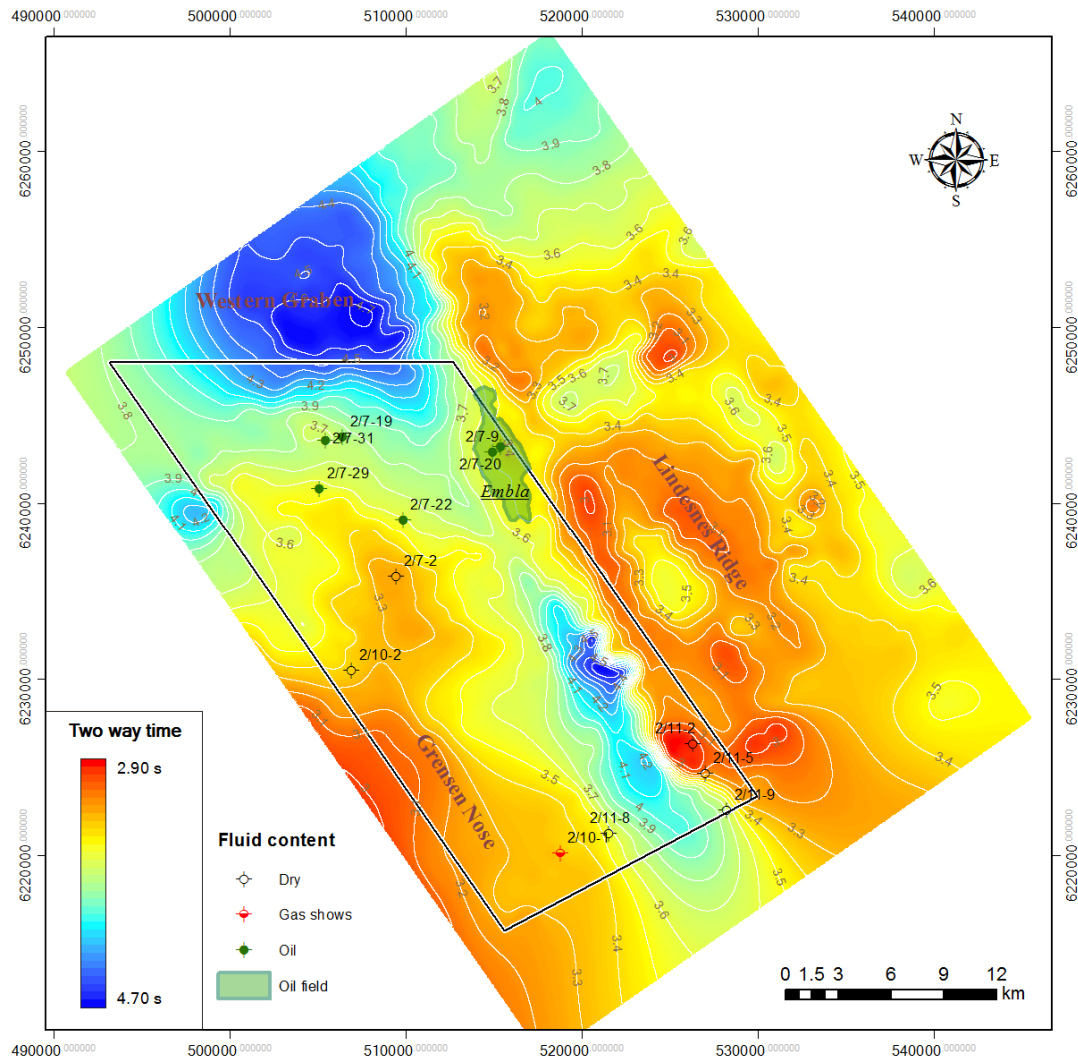

Figure 8. 2D seismic time structural map of BCU

(3) 2/7-22 well

A 14-m pay zone was interpreted from Devonian alluvial clean sands at 4435.5-4502.0 m interval, and the oil-water contact was predicted at 4502 m. One

DST test was performed at the 4489-4496 m interval and flowed 207 sm^3 of condensate and 347 sm^3 of water per day through a 12.7 mm choke.

(4) 2/7-29 well

Overall 160.5 m gross of sands were penetrated in the Upper Jurassic interval. A one-gallon dead-oil sample was obtained in the Eldifisk Formation sandstone. No DST was performed.

(5) 2/7-31 well

A DST was performed over the Upper Jurassic Ula Sandstone 4565.9-4623.8 m interval. The well flowed at an average stabilized rate of 283 sm^3 of oil and 120 000 sm^3 of gas on a 16/64" choke.

Wireline formation pressure tests were taken throughout the Permian Rotliegendes section. Oil samples were recovered from two FMT tests at 4793 m and 4812 m.

(6) 2/10-1S well

A gas kick appeared while drilling at 4343 m in the Permian Rotliegendes sand. A DST was planned to the Rotliegendes sand interval, but it was not carried out due to a leak in the casing.

3.2.2 Hydrocarbon in chalk reservoirs

Discoveries in Cretaceous to Paleocene chalk reservoirs were made in Eldfisk field, Valhall field, and Hod field. Hydrocarbons were tested by the 2/7-2, 2/7-31, and 2/11-2 wells, and oil shows were reported from the 2/7-9, 2/7-19, 2/11-5 and 2/11-9 wells (Figure 9).
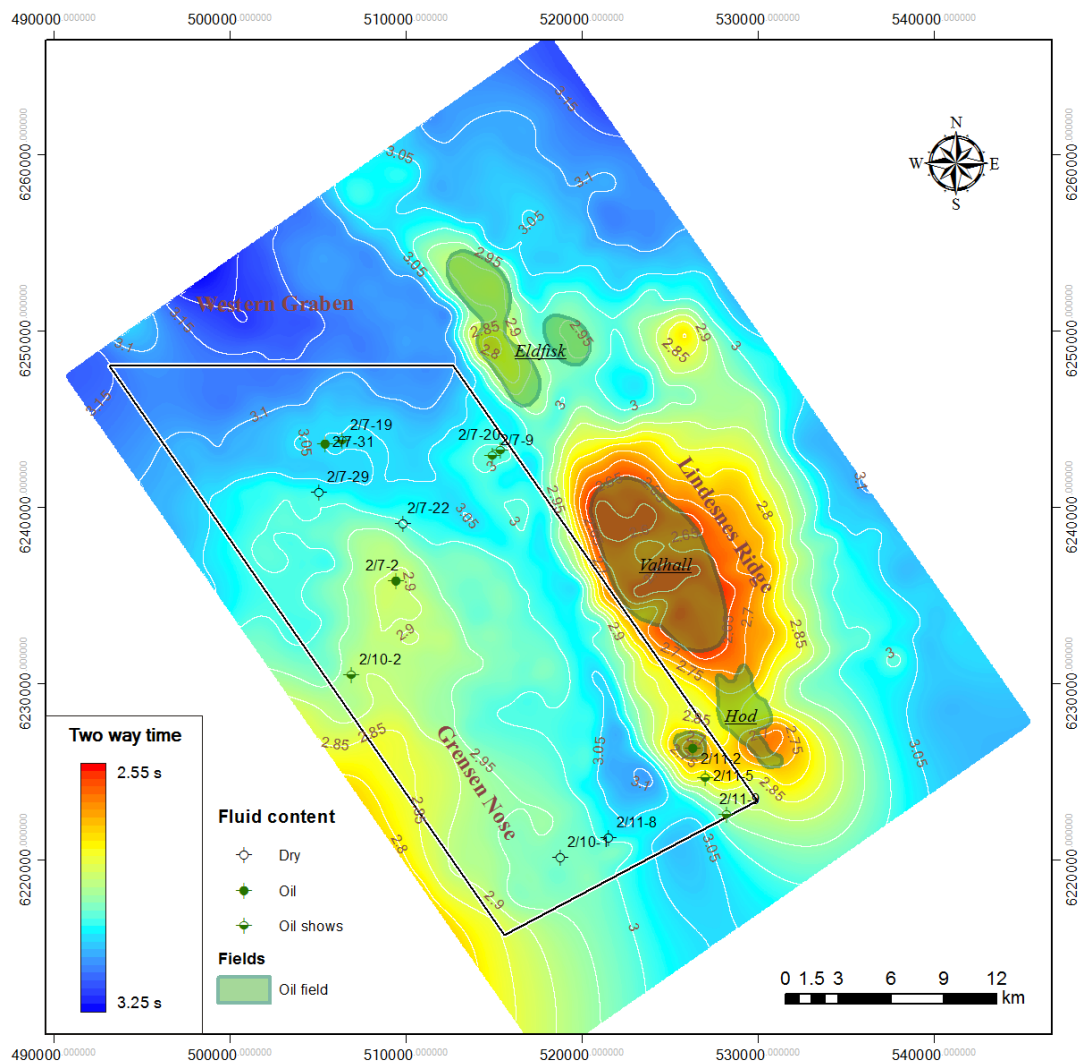
Figure 9. 2D seismic time structural map of Top Cretaceous

(1) 2/7-2 well

     Oil shows were observed on the 3013.9-3027.9 m cores in the Tor Formation. One DST was performed at 3005.3-3017.5 m interval of the uppermost Tor Formation. 6.83 m^3 load water and 0.68 sm^3 oil was flowed. After acidization, 54.6 sm^3 of oil, 44.7 m^3 of formation water, and 4814 sm^3 of gas were produced.

(2) 2/7-9 well

     Good shows were recorded in the Paleocene Danian limestone and Cretaceous Chalk intervals. However, no hydrocarbons were tested from either reservoir.

(3) 2/7-19 well

Some fluorescence was observed in the Late Cretaceous chalk reservoirs.

(4) 2/7-31 well

Hydrocarbon shows were recorded in the Lower Cretaceous Tuxen Formation.

(5) 2/10-2 well

Weak shows were reported in the Late Cretaceous Tor Formation from cores and cutting samples.

(6) 2/11-2 well

Quality oil-bearing chalk reservoirs were encountered in the Late Cretaceous Hod Formation below 2640.5 m. A 51.5-m net pay was estimated with average porosity of 27.7 % and an average water saturation of 40.3 %. Two runs of DST were carried out in the Hod Formation, both tests produced oil and gas, no water. The maximum flow rate was achieved while testing the 2642.6-2665.5 m interval, with 546 sm^3 of oil and 82 120 sm^3 of gas per day.

(7) 2/11-5 well

Fair dull golden fluorescence and fair cut were reported in the Upper Jurassic chalk reservoirs. However, these sections were found below the oil-water contact and no moveable hydrocarbons were presented.

(8) 2/11-9 well

Oil shows associated with fractures were observed in the Late Cretaceous chalk interval. Unfortunately, the quality of the chalk reservoirs was poor.

3.2.3 Hydrocarbon in Paleocene clastics

In the Paleogene section, some oil was tested in silty Oligocene shales from the 2/11-2 well, and frequent oil shows were reported in the upper part of the Paleogene of the 2/11-5 well (Figure 10).
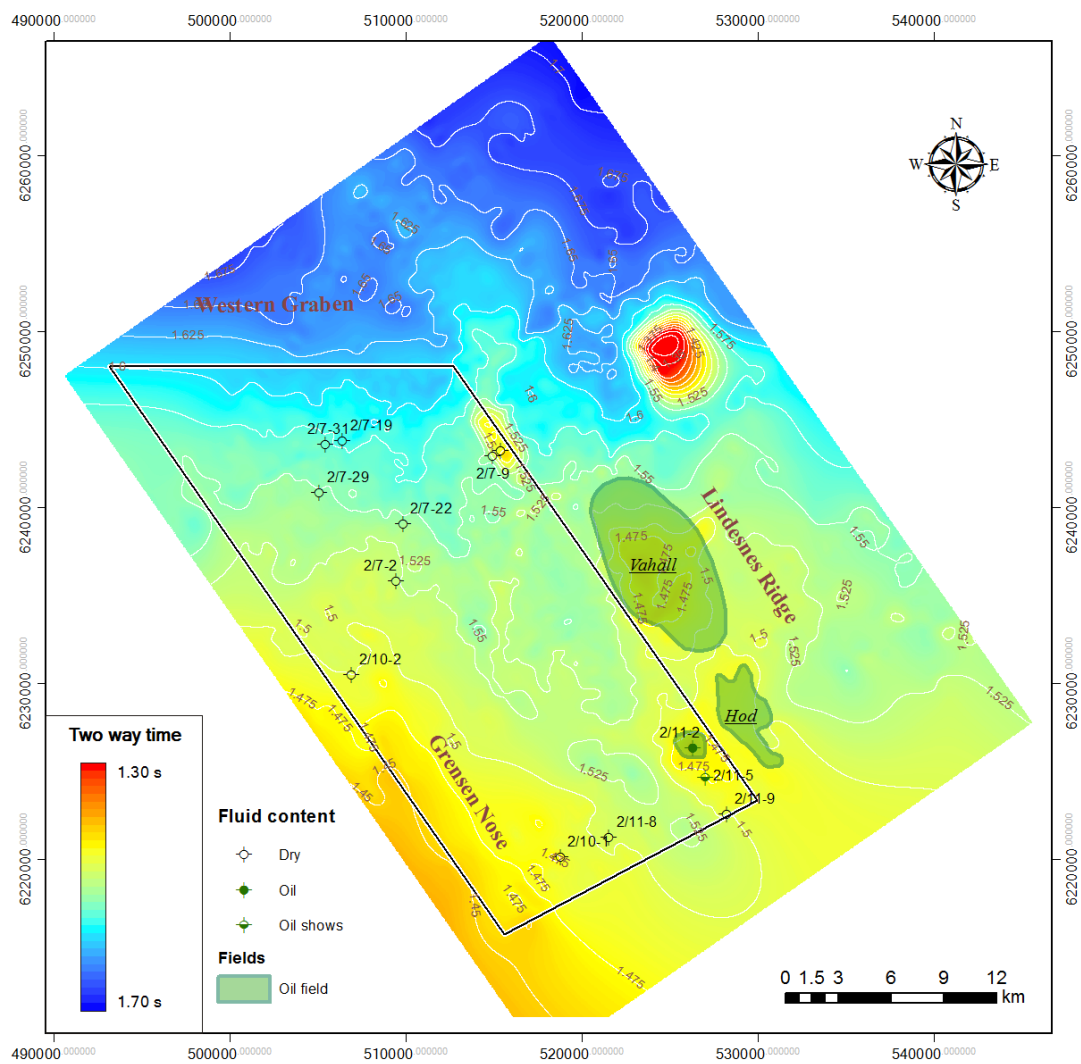
Figure 10. 2D seismic time structural map of Top Paleogene

(1) 2/11-2 well

High gas readings were recorded from approximately 1415 to 1675 m. Oil shows and free oil in the mud were recorded during the drilling.

(2) 2/11-5 well

Dull yellow fluorescence was recorded in Paleocene clastic intervals.

4 Seismic interpretation

4.1 Synthetics

The purpose of performing synthetic analysis is to construct the time-depth relationship between the well and seismic gather. Synthetic analysis has been carried out on normal-polarity seismic to the 2/7-2, 2/7-9, 2/7-19, 2/7-22, 2/7-29, 2/7-31, 2/10-1S, 2/10-2, 2/11-2, 2/11-5, 2/11-8, and 2/11-9 wells.

Taking the synthetics of the 2/7-31 well for example, Paleocene Balder Formation consists of laminated fissile shale with interbeded sandy tuffs and occasional stringers of carbonates (Deegan et al., 1977), and its formation top is represented by a strong peak on synthetic profile; Upper Cretaceous is composed of chalky limestone, and the formation top is featured by a strong peak reflection; an significant trough reflection is featured along the BCU (Figure 11).
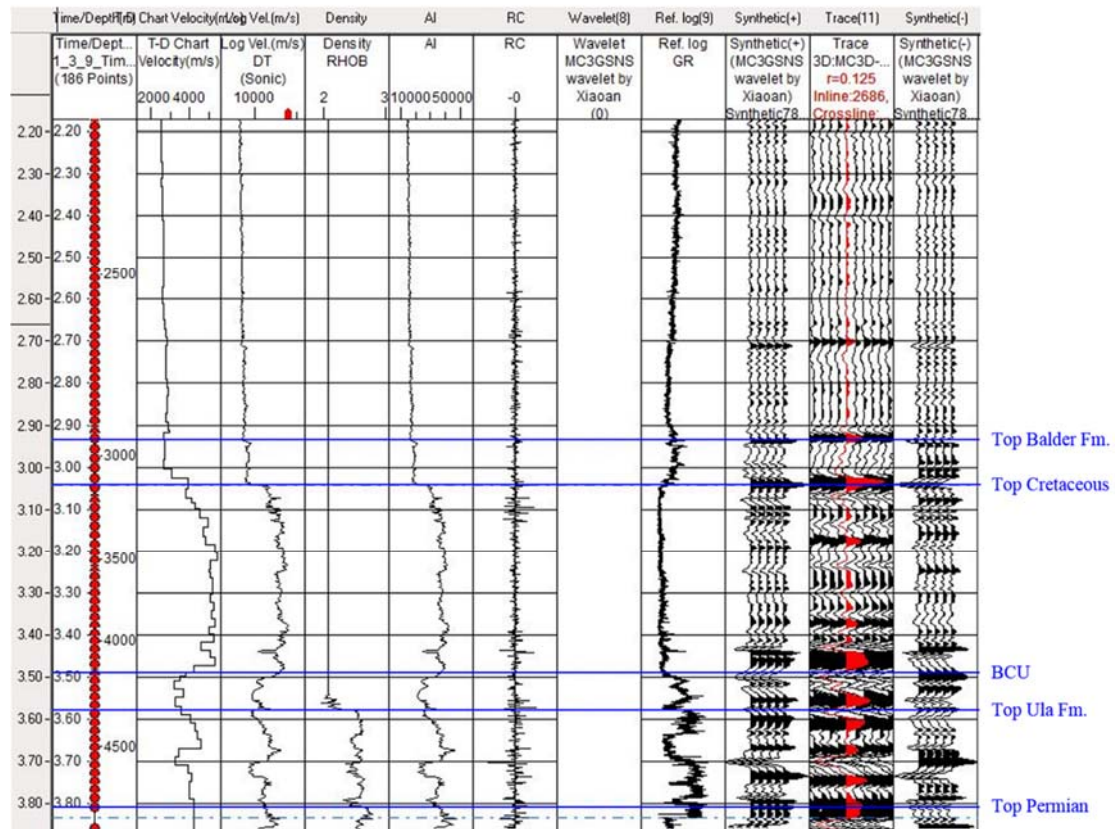

Figure 11. Synthetic profile of 2/7-31 well

4.2 Regional cross sections

Separated by the horst between Grensen Nose and Lindesnes Ridge, the Western Graben comprises northern and southern sub-sags by complex tectonic movements. Seismic reflection above the Lindesnes Ridge shows "pushed-down" anomaly, gas bright spot, and chaotic events by interference of gas contents surrounding the 2/11-2 well location (Figure 12; line location see Figure 6).
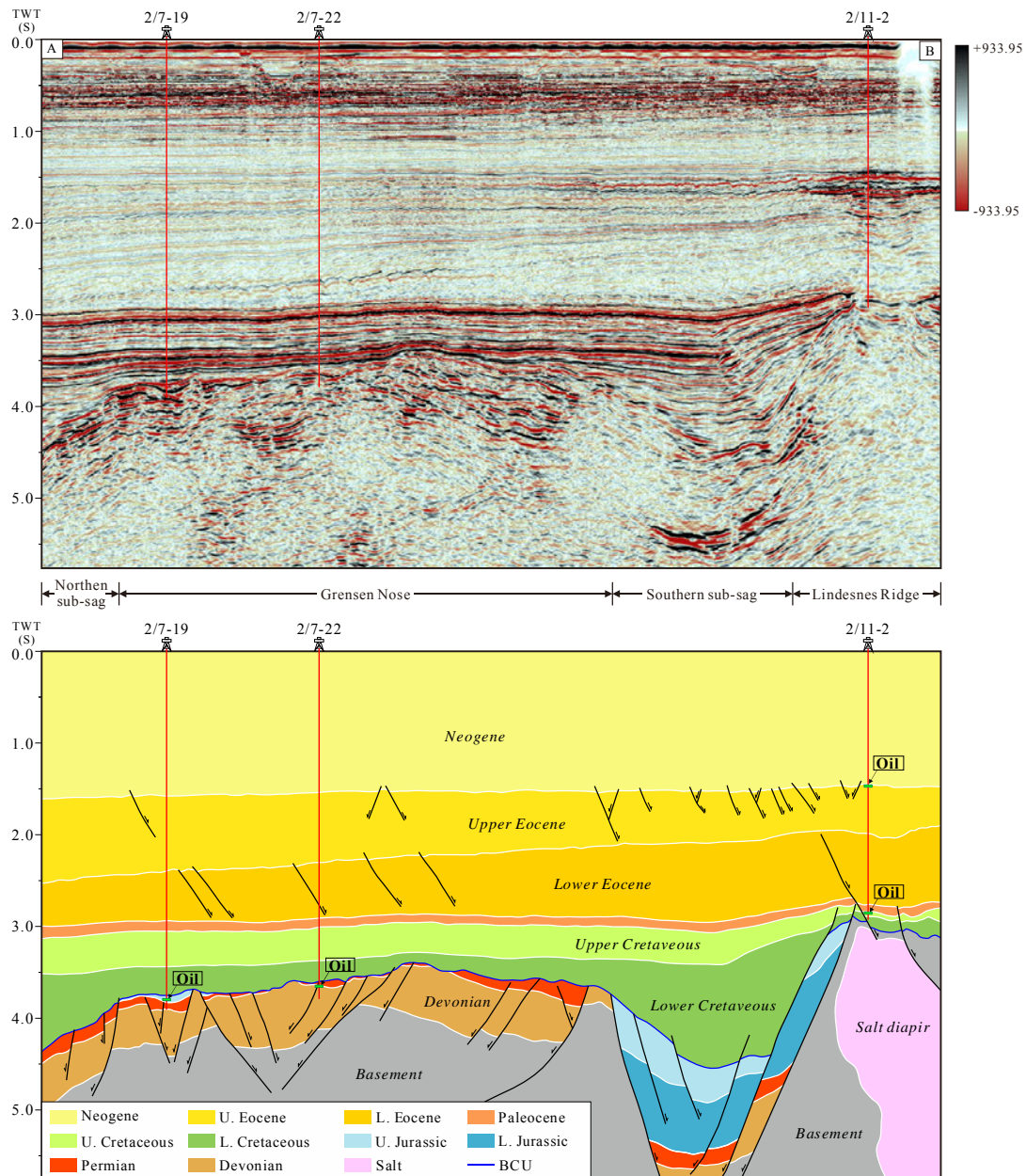

Figure 12. Seismic and geological sections through 2/7-19, 2/7-22, and 2/11-2 wells

Several sets of normal faults were developed through the Devonian-Jurassic, Early Eocene, and Late Eocene episodes. These moderate to high angle faults indicates significant rifting events during above critical stages.

Jurassic sediments were poorly deposited on the Grensen Nose due to limited accommodation space on the uplift high. In the Upper Jurassic Ula Formation sand unit of the 2/7-19 well, hydrocarbon was tested in the 4711-4838 m interval.

Devonian and Permian were partly eroded on the Grensen Nose during end Jurassic compression and erosion. The 2/7-22 well tested hydrocarbon from 4484-4491 m interval sandstone.

Salt diapirism in southern North Sea was induced by the Upper Permian Zechstein salt intrusion, and it has contributed several anticlines on the Lindesnes Ridge. The 2/11-2 well flowed hydrocarbon from Cretaceous chalk reservoirs and Late Eocene clastic sands.

4.3 Structural mapping

Structural grids including the BCU, base of Cretaceous chalk, Top Cretaceous, Top Balder Formation, and Top Paleogene have been interpolated based on 3D seismic interpretation. Utilizing the velocity model of time-depth curves from well synthetics, all grids have been converted into depth domain.

The depth structural map of the BCU shows two separated sub-sags which are oriented towards NW-SW direction, and the maximum buried depth of the BCU reached 5619 m (Figure 13).
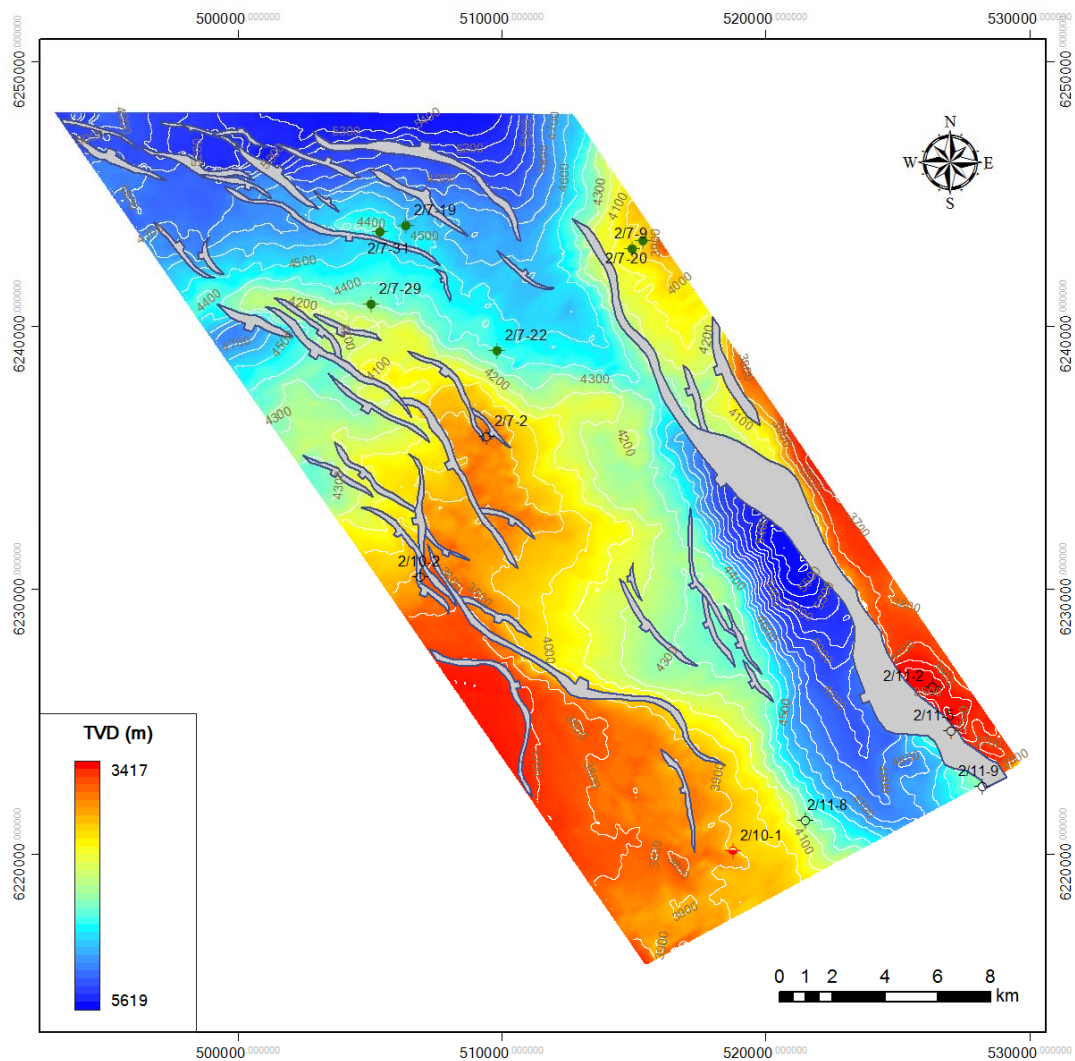

Figure 13. Depth-structure contour map of the BCU

In the Western Graben of southern area, normal faults generally strike along SE-NW direction, while they are oriented towards SEE-NWW direction in its northern part. A three-way closure is mapped at the 2/7-19 and 2/7-31 well location, from which hydrocarbons were tested in the Upper Jurassic Ula sandstone. However, no obvious structure-related closures were mapped for the rest of the oil wells, such as the 2/7-29 and 2/7-22 wells, which indicates that hydrocarbon may be entrapped within stratigraphic closures.

The depth structural map at the base of Cretaceous chalk inherited structural geometry from the BCU, however, the southern sub-sag has been shrunk drastically (Figure 14). The 2/7-31 well is located in a minor anticline and encountered hydrocarbon shows from the Lower Cretaceous Tuxen Formation sandstone.
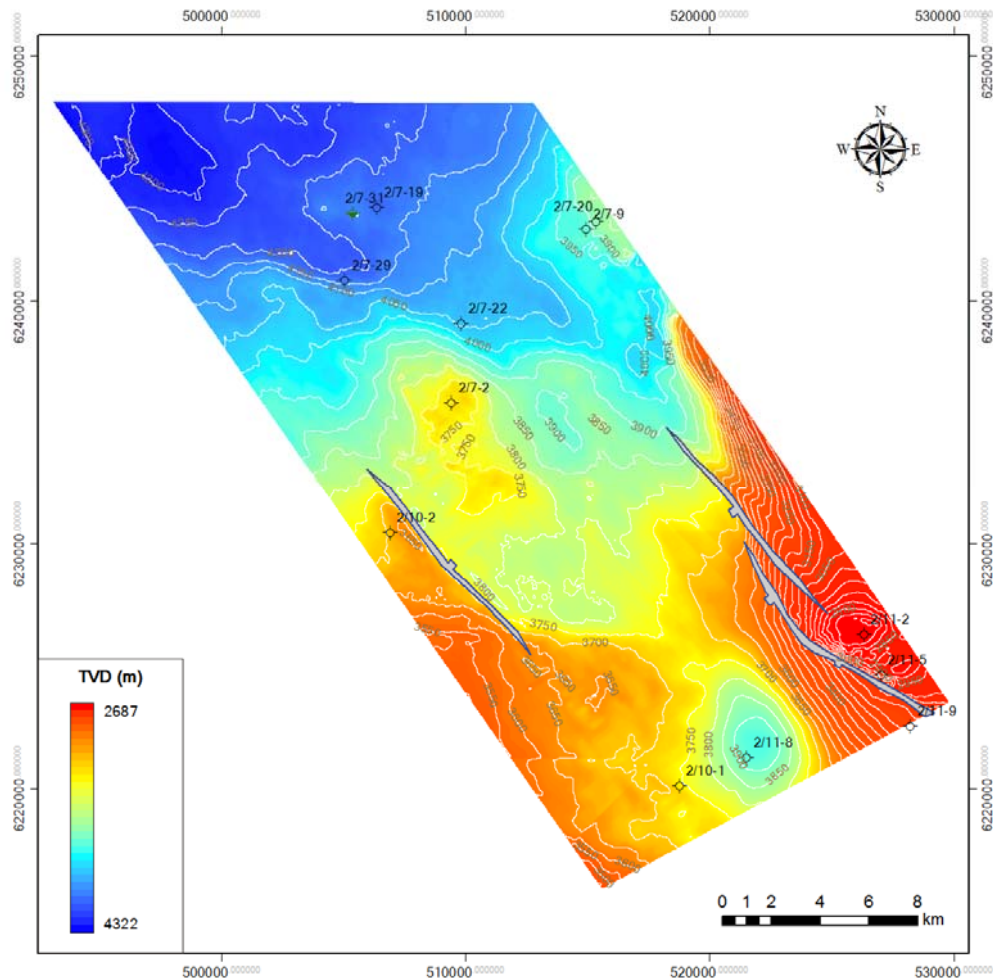

Figure 14. Depth-structure contour map of the base of Cretaceous chalk

22

At least three four-way closures had been developed by salt diapirism on the depth structural map of Top Cretaceous (Figure 15). Hydrocarbons were tested from Cretaceous chalks, such as the 2/7-2 well, Embla Field (2/7-9 well located), and Hod Field (2/11-2 well located). In the Hod Field, the 2/11-5 and 2/11-9 wells were drilled below oil-water contact. Occasional hydrocarbon shows were reported from the 2/7-19 and 2/10-2 wells, where no significant closures were developed. These minor fingerprints from hydrocarbon shows can be explained by hydrocarbons having migrated through fractures or pores within chalk reservoirs and then escaped to shallower layers.
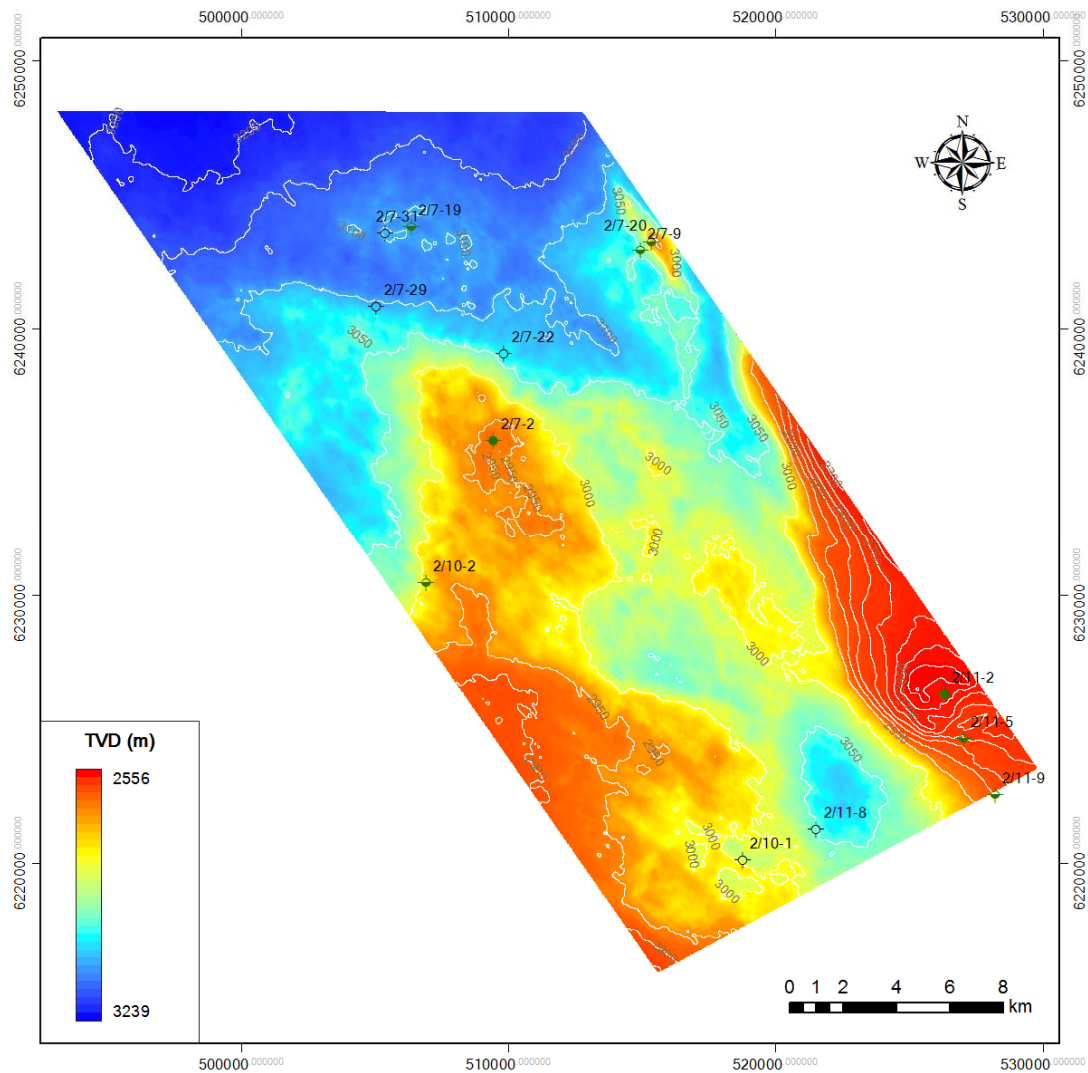

Figure 15. Depth-structure contour map of Top Cretaceous

The buried depth of Paleocene Top Balder Formation ranges between 2475 and 3068 m (Figure 16). Hydrocarbon was reported from the 2/7-9, 2/11-2, and 2/11-5 wells, which are located in four-way anticlines induced by salt. There is a low-relief four-way closure in the 2/7-2 well location, however, no hydrocarbon was found.
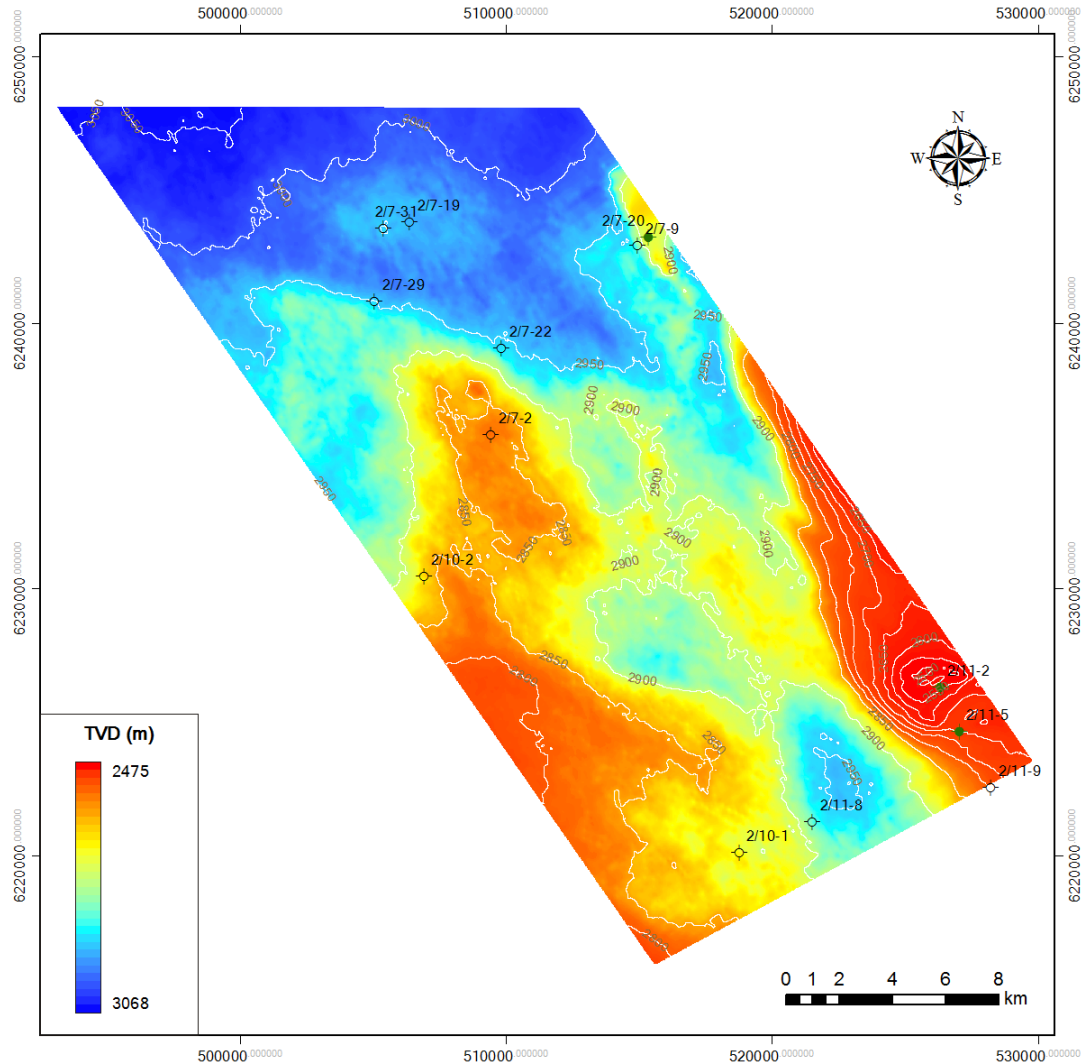
Figure 16. Depth-structure contour map of Top Balder Formation, Paleocene

The top of Paleogene has a 186 m of relief (1404-1590 m) throughout the structure. Hydrocarbons were encountered in salt-induced anticlines, which comprise more than 50 m of relief. Enormous tortoise-shell pattern faults had been developed in the shallower sections while rifting, and they produced dense and irregular features on the grid of contour structural map (Figure 17).
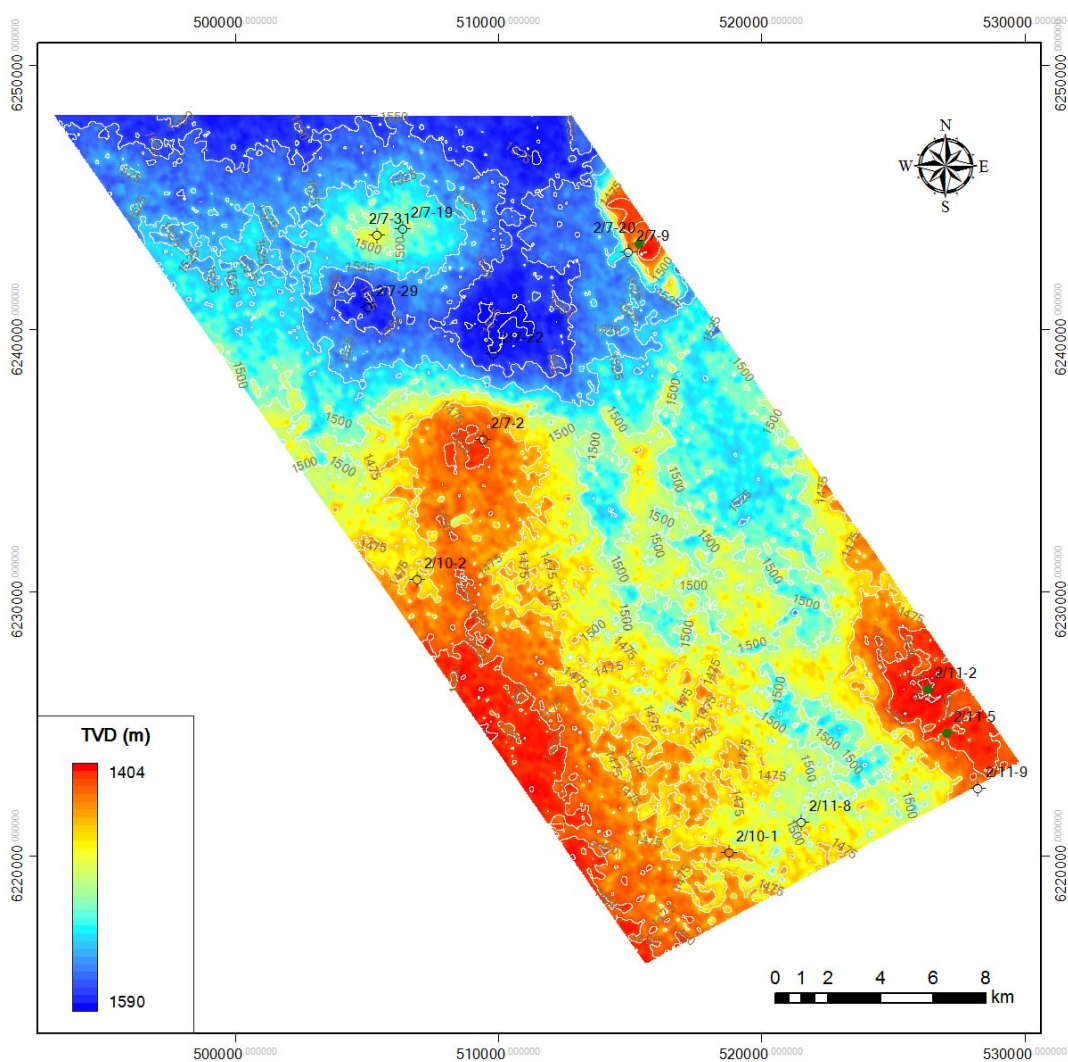
Figure 17. Depth-structure contour map of Top Shetland Group, Paleogene

According to the relationship between discovered wells and seismic interpretation, it is concluded that:

(1) For the clastic sections beneath the BCU, hydrocarbons had been found in either structure-related faulted blocks or stratigraphy-entrapped closures; and

(2) For the strata above the BCU, hydrocarbons were generally preserved by salt-induced closures.

Consequently, it is necessary to perform seismic attribute analysis to characterize fluid responses and explore favorable petroliferous prospects.
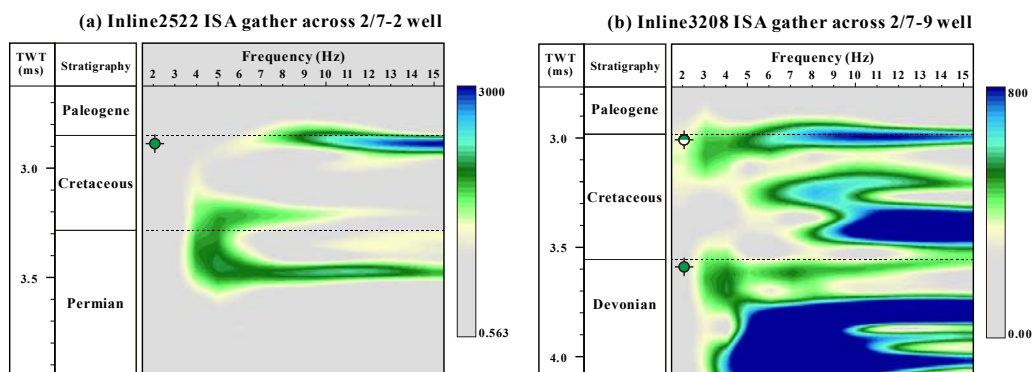
5 Low-frequency seismic analysis

5.1 Low-frequency spectra

The ISA cube is constructed with the idea that constituting a series of spectral sections, which contain variable frequencies along specific seismic lines, either inline or crossline direction. In practice, users define the increment of frequency increment, and spectral sections can be produced for each individual frequency. Eventually, these spectral sections can be integrated into a cube. In an ISA cube, one direction displays the instantaneous spectrum of a certain frequency, the other direction shows instantaneous spectra along increasing frequencies.
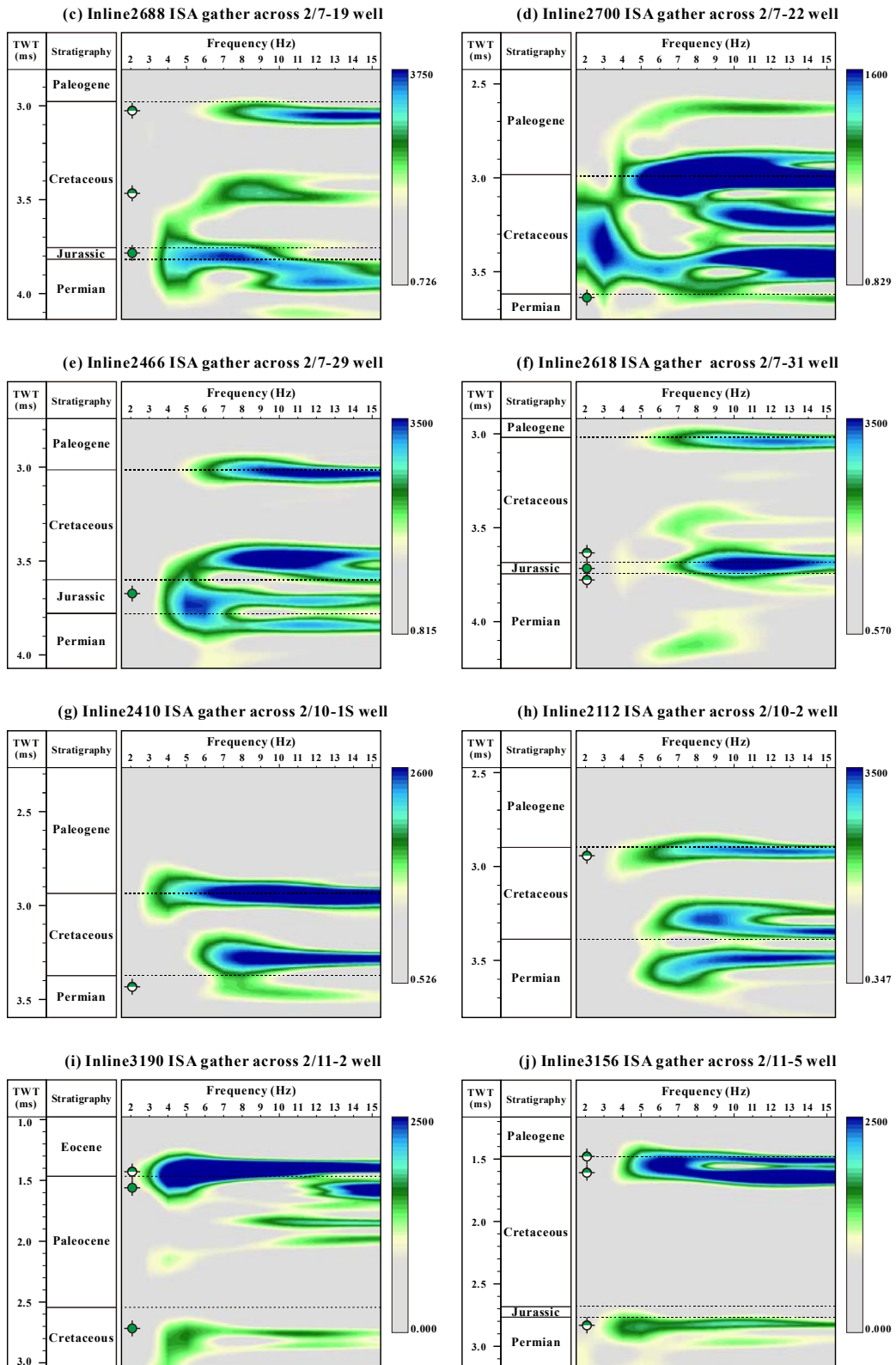
ISA cubes are generated for seismic lines crossing penetrated wells, frequency are observed from 2 to 15 Hz, and the step of frequency increment is 1 Hz.

The 2/7-2 well tested hydrocarbons from Late Cretaceous Tor Formation (see green symbol in Figure 18a). On the ISA gather crossing the well, significant amplitudes are observed from 6 to 15.5 Hz. The maximum magnitude of attribute peak is listed in Table 2, the same as the rest of wells.

The 2/7-9 well tested hydrocarbon from Devonian sands, and recorded oil shows from the Late Cretaceous Ekofisk Formation chalk reservoirs. The significant amplitudes are observed from 3 to 15.5 Hz. The attribute peaks for above reservoirs appear at 7 and 11 Hz, respectively (Figure 18b).

(Figure to be continued)

26

(c) Inline2688 ISA gather across 2/7-19 well

(d) Inline2700 ISA gather across 2/7-22 well

(e) Inline2466 ISA gather across 2/7-29 well

(f) Inline2618 ISA gather across 2/7-31 well

(g) Inline2410 ISA gather across 2/10-1S well

(h) Inline2112 ISA gather across 2/10-2 well

(i) Inline3190 ISA gather across 2/11-2 well

(j) Inline3156 ISA gather across 2/11-5 well
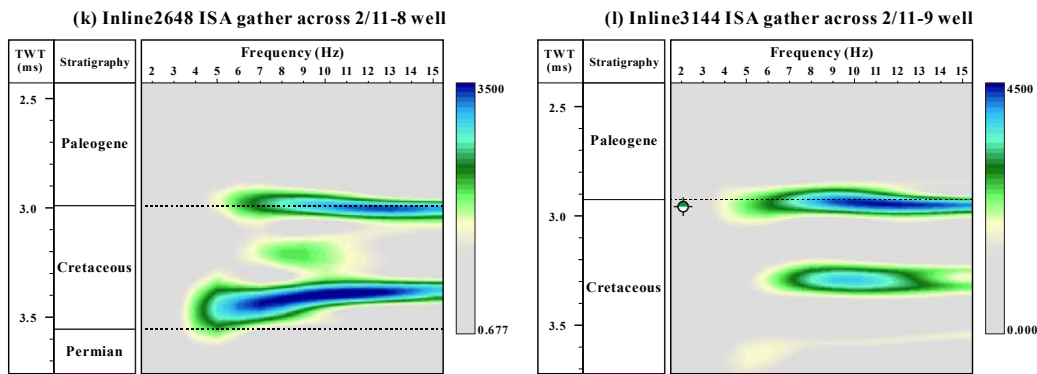
(Figure to be continued)

27

Figure 18. ISA gather with frequencies from 2Hz to 15 Hz at the well location

(⊕ : oil tested; ⊕: oil shows recorded)

The 2/7-19 well tested hydrocarbon from the Late Jurassic Ula Formation sandstone, and recorded oil shows from Late Cretaceous Hidra Formation and Tor Formation chalk reservoirs. Significant amplitudes for the Late Jurassic pay zone are observed from 3 to 10 Hz. The attribute peaks for above reservoirs appear at 7 , 8, and 13 Hz, respectively (Figure 18c).

The 2/7-22 well tested hydrocarbon from Devonian sands. significant amplitudes for the pay zone are observed from 6 to 15Hz, and the attribute peaks for the reservoirs appear at 15 Hz (Figure 18d).

The 2/7-29 well tested hydrocarbon from the Late Jurassic Eldfisk Formation sandstone. Significant amplitudes for the pay zone are observed from 4 to 15 Hz, and the attribute peak appears at 5 Hz (Figure 18e).

The 2/7-31 well tested hydrocarbon from Late Jurassic Ula Formation sands, and recorded oil shows from Early Cretaceous Tuxen Formation chalk and Early Permian Rotliegendes sandstone. Significant amplitudes for the pay zones are observed from 6 to 15 Hz, and the attribute peaks for above reservoirs appear at 11, 9, and 11 Hz, respectively (Figure 18f).

The 2/10-1S well encountered a gas kick from Permian Rotliegendes sandstone. Significant amplitudes for Rotliegendes sand are observed from 6 to 14 Hz, and the attribute peaks for the reservoir appears at 10 (Figure 18g).

28

The 2/10-2 well reported oil shows from Late Cretaceous Tor Formation chalk reservoirs. Significant amplitudes for the reservoirs are observed from 4 to 15 Hz, and the attribute peak appears at 12 Hz (Figure 18h).

The 2/11-2 well tested hydrocarbon from Late Cretaceous Hod Formation chalk and Paleocene Hordaland Group clastic reservoirs. Significant amplitudes for the pay zones are observed from 3 to 15 Hz, and the attribute peaks for above reservoirs appear at 5 and 8 Hz, respectively (Figure 18i).

The 2/11-5 well encountered oil shows from Late Cretaceous Ekofisk Formation chalk and Paleocene Hordaland Group clastic reservoirs. Significant amplitudes for reservoirs are observed from 3 to 15 Hz, and the attribute peaks for above reservoirs appear at 9 and 6 Hz, respectively (Figure 18j).

Although two attribute peaks show on the ISA gather across the 2/11-8 well, there was no hydrocarbon was encountered and reported. These attribute anomalies might be related to variation of fluid saturation between different lithologies (Figure 18k).

The 2/11-9 well recorded oil shows from Late Cretaceous Ekofisk Formation chalk reservoirs. Significant amplitudes for the reservoir are observed from 4 to 15 Hz, and the attribute peak appears at 12 Hz (Figure 18l).

The above observations conclude that low-frequency spectra show significant indications of when reservoirs are saturated with hydrocarbon. However, it is difficult to designate one or two frequency bands to be the best representation specifically. Instead, all bands from low-frequency range (< 15 Hz) may have potential probabilities of showing abnormal frequency responses.

Table 2. Attribute peaks on petroliferous sections across key wells

No.	Well	ISA volume		Content	Petroliferous section		Attribute peak	
		Inline	Crossline		Age	Group/Formation	Frequency	Numeric magnitude
1	2/7-2	2522		Oil	Late Cretaceous	Tor Fm	15Hz	2764
2	2/7-9	3208		Oil	Devonian		7Hz	523
				Oil shows	Late Cretaceous	Ekofisk Fm	11Hz	617
3	2/7-19	2688	3306	Oil	Late Jurassic	Ula Fm	7Hz	3630
				Oil shows	Late Cretaceous	Hidra Fm	8Hz	2749
						Tor Fm	13Hz	3828
4	2/7-22	2700		Oil	Devonian		15Hz	970
5	2/7-29	2466	3176	Oil	Late Jurassic	Eldfisk Fm	5Hz	3332
6	2/7-31	2618		Oil	Late Jurassic	Ula Fm	9Hz	1933
				Oil shows	Early Cretaceous	Tuxen Fm	11Hz	3837
				Oil shows	Early Permian	Rotliegendes Gp	11Hz	1766
7	2/10-1S	2410		Gas shows	Permian	Rotliegendes Gp	10Hz	1988
8	2/10-2	2112		Oil shows	Late Cretaceous	Tor Fm	12Hz	3307
9	2/11-2	3190		Oil	Late Cretaceous	Hod Fm	5Hz	1645
				Oil	Paleocene	Hordaland Gp	8Hz	4617
10	2/11-5	3156		Oil shows	Late Cretaceous	Ekofisk Fm	9Hz	1822
				Oil shows	Paleocene	Hordaland Gp	6Hz	2744
11	2/11-8	2648		Dry				
12	2/11-9	3144		Shows	Late Cretaceous	Ekofisk, Tor and Hod Fm	12Hz	4430

Notes: Fm-Formation; Gp-Group

30

5.2 Frequency responses on wells

To illustrate the relationship between low-frequency shadow effects and fluid mobility, it is critical to find evidence from spectral sections through discovered wells.

Spectral profiles for the 2/7-2, 2/7-19, 2/7-22, 2/7-29, and 2/7-31 wells along the crossline direction of the seismic survey were extracted. For the 2/10-2 well, the profile was extracted along the inline direction (Figure 19).
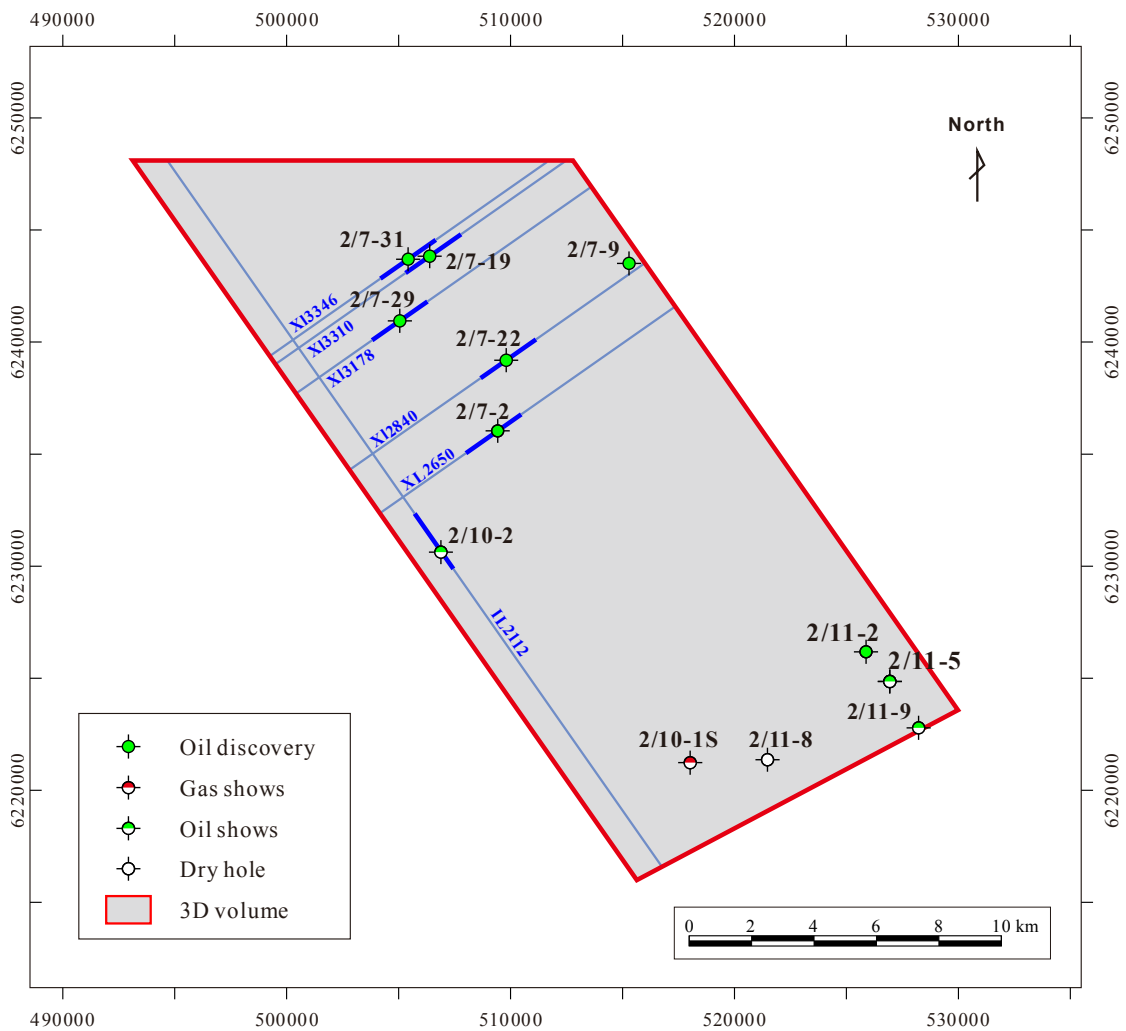

Figure 19. Seismic lines for spectral sections through key wells

31

The 2/7-2 well tested hydrocarbon in the uppermost part of the Late Cretaceous Tor Formation with more than 40% of water after acidization. The pay zone shows amplitude anomalies on the 12, 15.5, and 20 Hz spectral sections (Figure 20). Amplitude anomaly for pay zone faded out on the 30 and 40 Hz spectral sections, and the amplitude anomaly appears below the pay zone on the 40 Hz section.
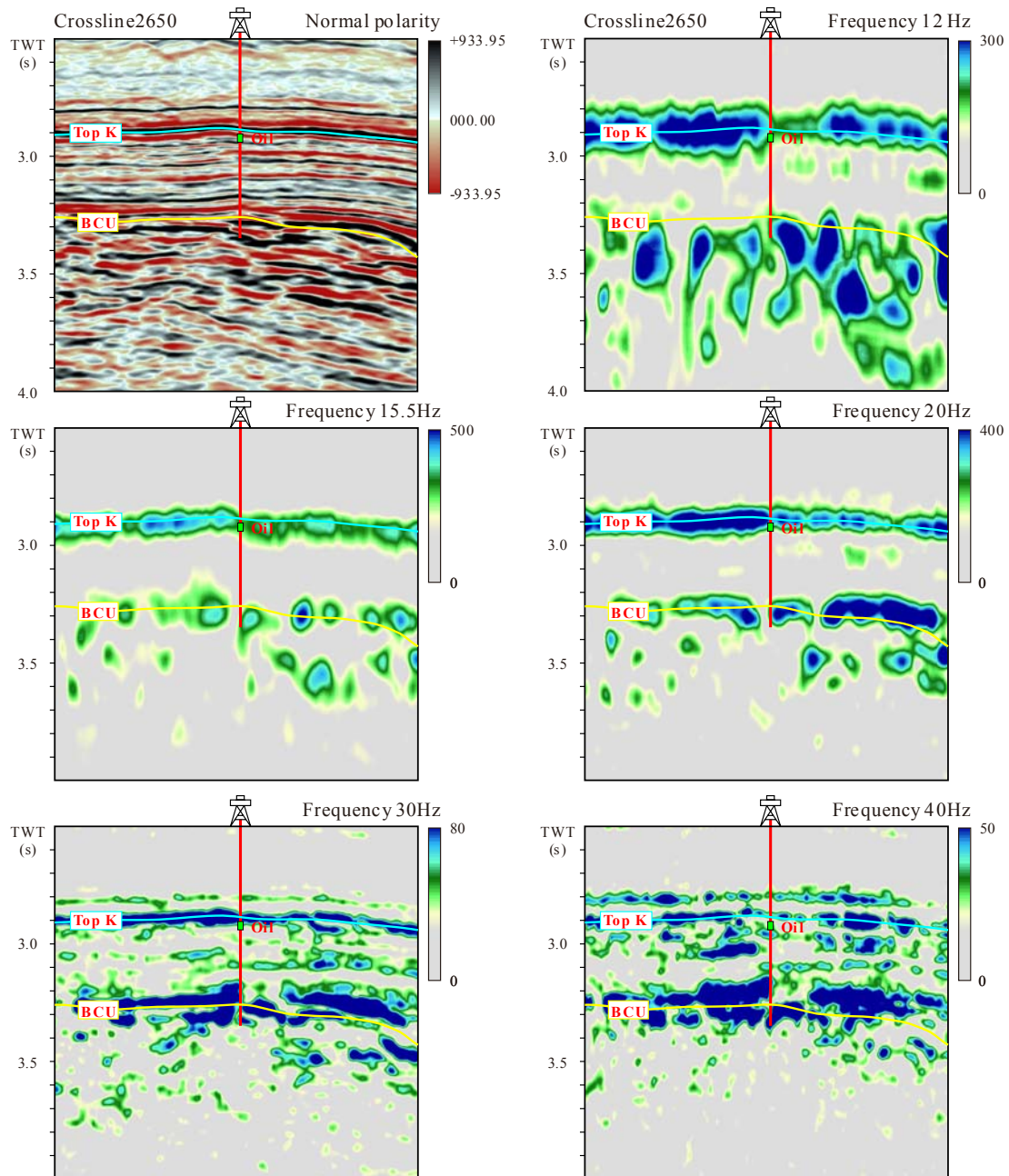

Figure 20. XL2650 spectral sections corresponding to the stacked seismic profile

32

The 2/7-19 well tested hydrocarbon in the Upper Jurassic Ula Formation. The pay zone shows amplitude anomalies on the 12 and 15.5 Hz spectral sections (Figure 21). Amplitude anomaly for pay zone faded out on the 20, 30, and 40 Hz spectral sections, but the amplitude anomaly appears either above or beneath the pay zone on these sections.
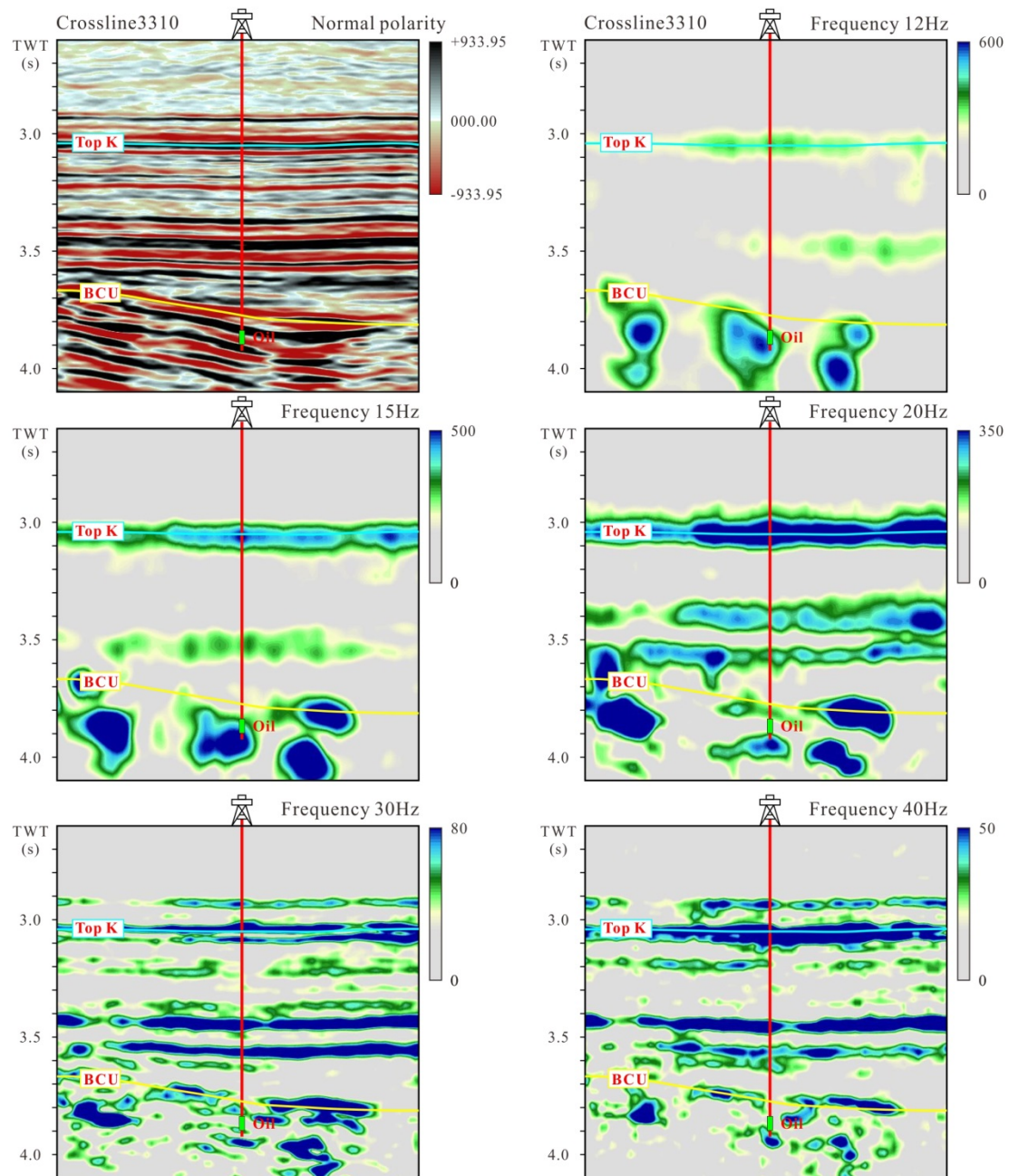

Figure 21. XL3310 spectral sections corresponding to the stacked seismic profile

33

The 2/7-22 well tested hydrocarbon in the Devonian alluvial clean sands. The pay zone is located on the edge of anomalies on the 12, 15.5, and 20 Hz spectral sections (Figure 22). Amplitude anomaly for pay zone persists to higher frequency sections, such as 30 and 40 Hz, but the amplitude anomaly appears above the pay zone on these sections.
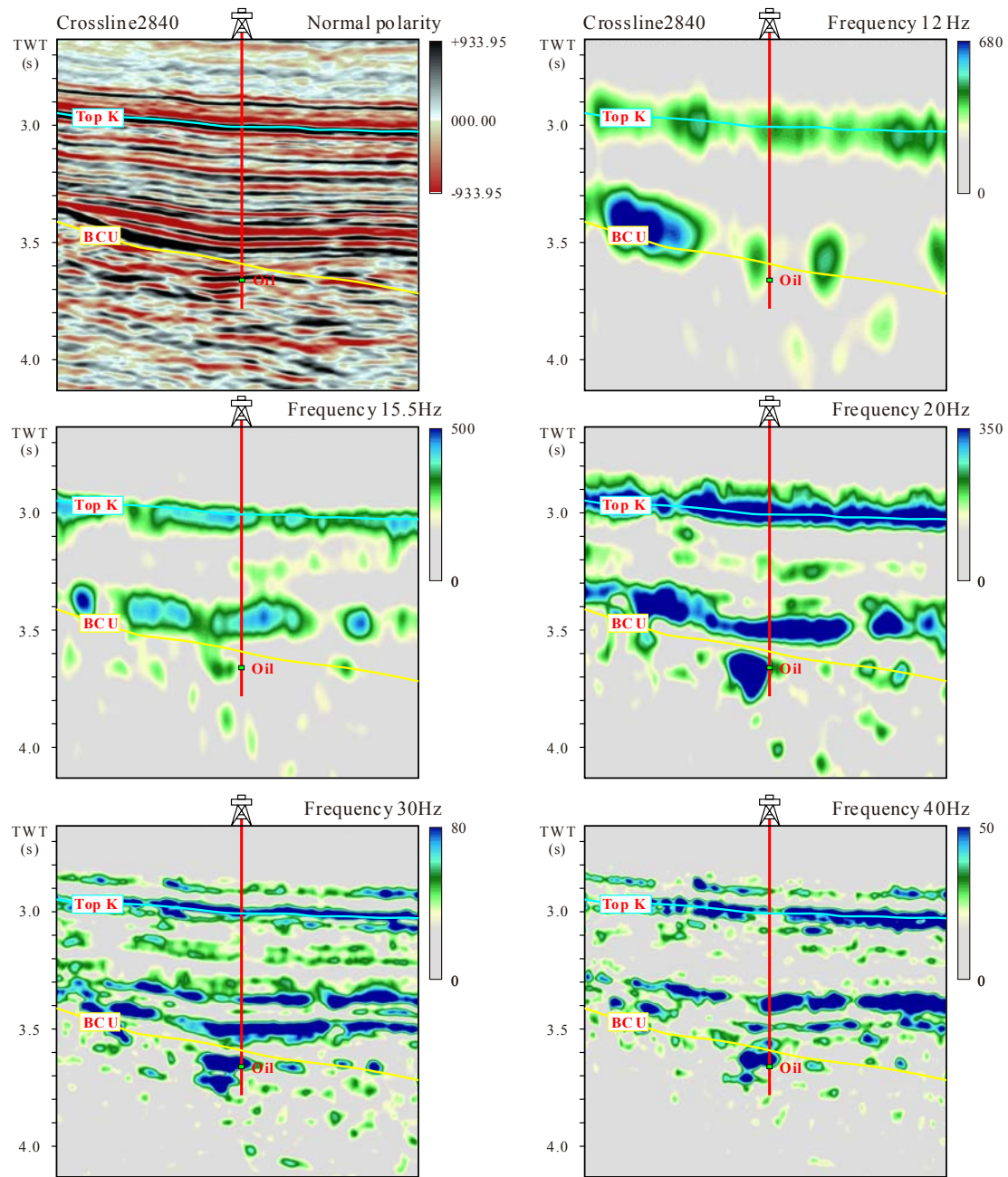

Figure 22. XL2840 spectral sections corresponding to the stacked seismic profile

The 2/7-29 well tested hydrocarbon in the Devonian alluvial clean sands. The pay zone is located on the edge of anomalies on the 7.2 and 15.5 Hz spectral sections (Figure 23). Amplitude anomaly for pay zone faded out on the 20, 30, and 40 Hz spectral sections, but the amplitude anomaly appears above the pay zone on these sections.
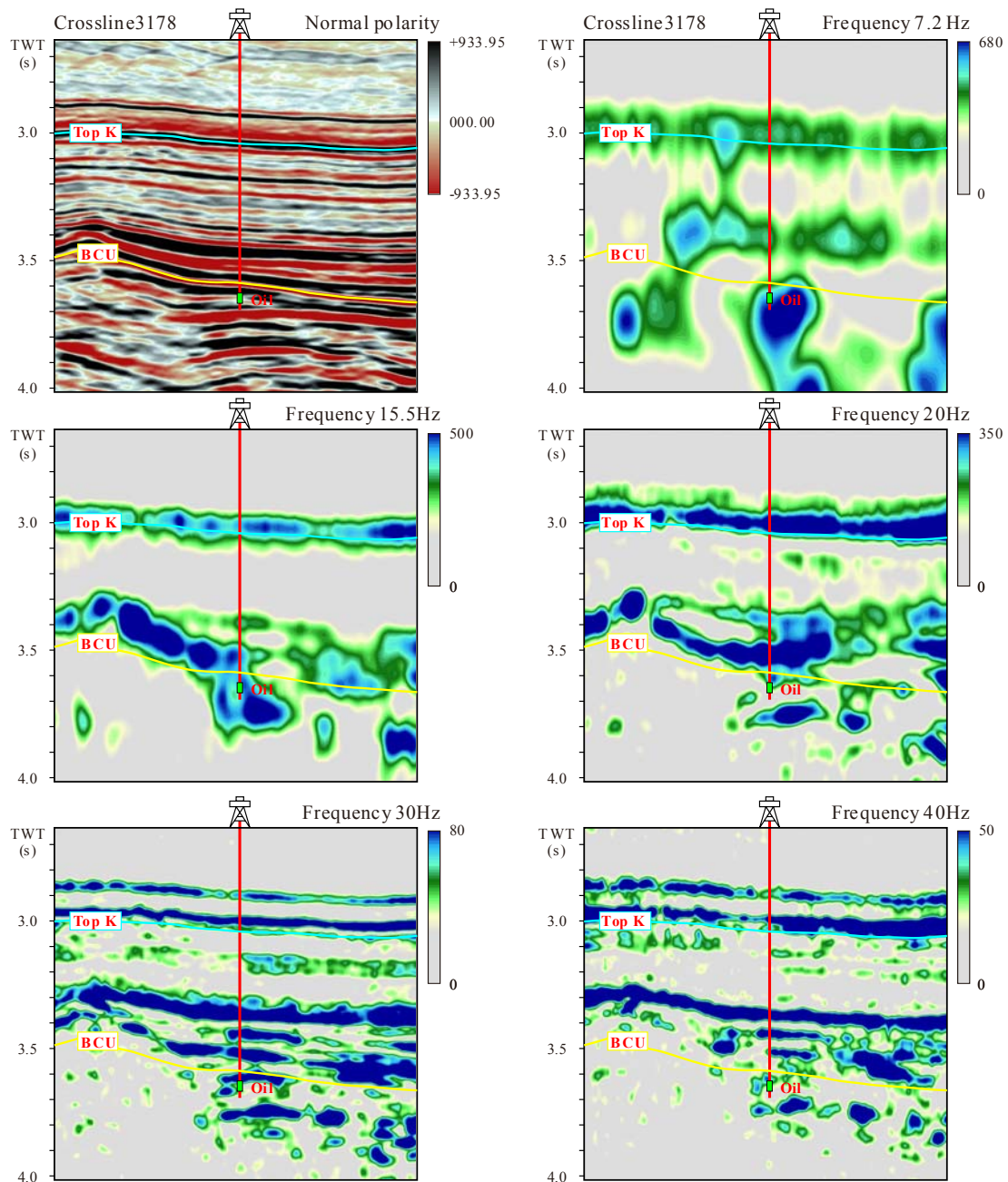

Figure 23. XL3178 spectral sections corresponding to the stacked seismic profile

The 2/7-31 well tested hydrocarbon in the Upper Jurassic Ula Sandstone. The pay zone is located on the edge of anomalies on the 12 and 15.5 Hz spectral sections (Figure 24). Amplitude anomaly for pay zone faded out on the 20, 30, and 40 Hz spectral sections, but the amplitude anomaly appears both above and below the pay zone on these sections.
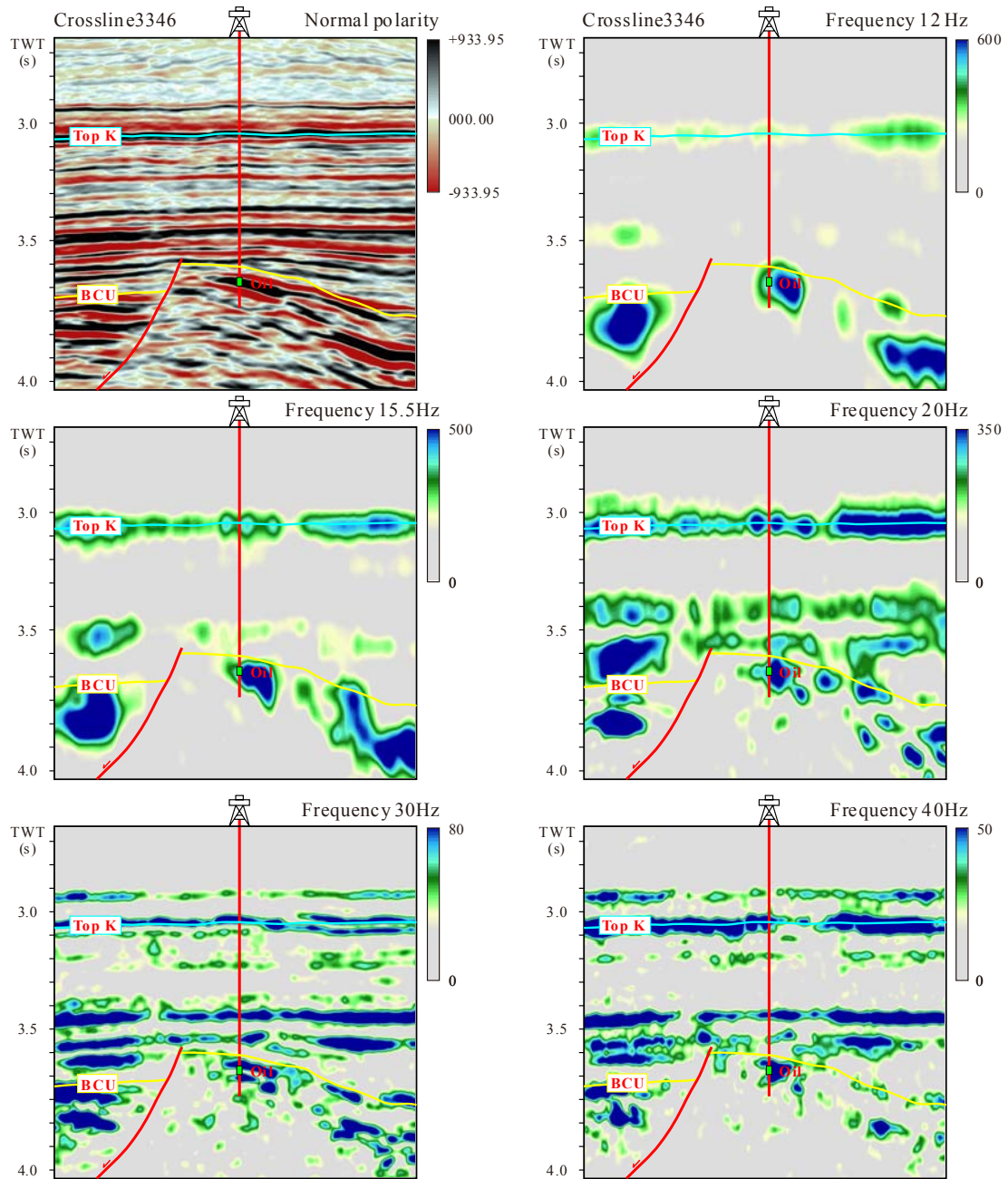

Figure 24. XL3346 spectral sections corresponding to the stacked seismic profile

The 2/10-2 well encountered Late Cretaceous Tor Formation, and there are no significant amplitude anomalies on spectral sections for chalk reservoir zones (Figure 25).
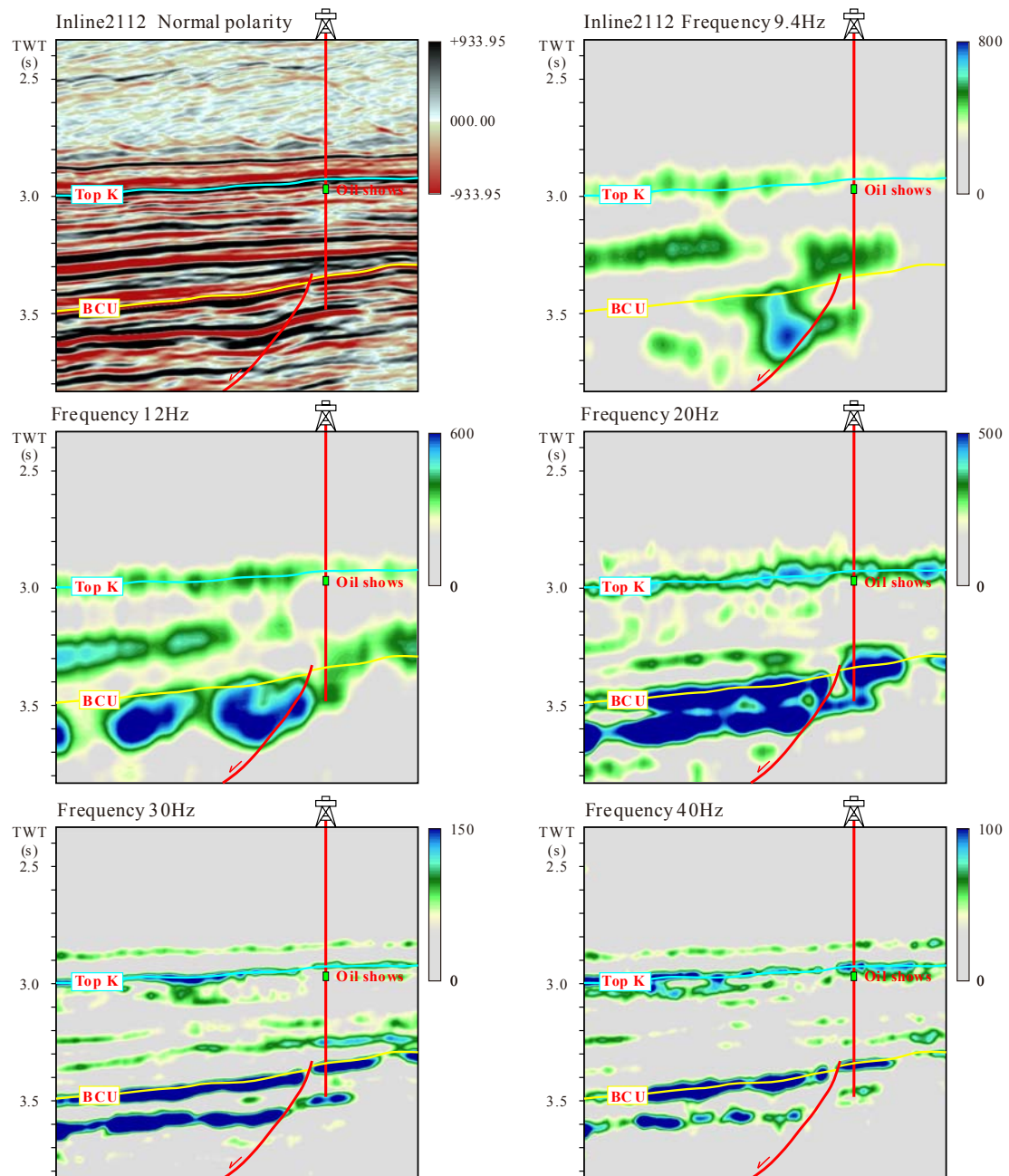

Figure 25. IL2112 spectral sections corresponding to the stacked seismic profile

The significant amplitudes spectral profiles show that low-frequency seismic presents significant anomalies for the fluid saturated sections, and high-frequency signals attenuated while propagating through pay zones. Consequently, considering amplitude anomaly features for further prospects, possible pay zones can be identified based on the following conditions:

(1) Low-frequency spectra often show amplitude anomalies;

(2) High-frequency spectra are usually attenuated drastically; and

(3) Amplitude anomalies may appear either above or below or to the side of petroliferous sections.

5.3 Frequency responses along horizons

To analyze frequency responses along the BCU, Top Cretaceous, and Top Paleogene, significant amplitudes attributes have been extracted from time-frequency envelopes of 4.8, 7.2, 9.4, 12, 15.5, 20, 30, 40, and 50 Hz. Each slice calculated the mean value of the envelope within a specific window, for instance, 200ms was involved below the BCU, 200ms was designated below Top Cretaceous, and 180ms was considered below Top Paleogene.

Considering penetrated wells show various attribute peak responses from arbitrary frequency range in pay zones, frequency attribute slices were classified into three categories, which are low-frequency attribute, medium-frequency attribute, and high-frequency attribute.

The low-frequency attribute slice was integrated by attributes of 4.8, 7.2, 9.4, 12, and 15.5 Hz slices, and it was normalized with the following algorithm:

$$A_{Low} = \frac{1}{5} \sum \frac{A_i}{Max(A_i)} \quad (i \ for \ 4.8, 7.2, 9.4, 12, and \ 15.5 \ Hz)$$

The medium-frequency attribute slice comprises attributes of 20 and 30 Hz slices, and it was normalized with the following algorithm:

$$A_{Medium} = \frac{1}{2} \sum \frac{A_i}{Max(A_i)} \quad (i \ for \ 20 \ and \ 30 \ Hz)$$

The high-frequency attribute slice was computed by 40 and 50 Hz slices, and it was normalized with the following algorithm:

$$A_{High} = \frac{1}{2} \sum \frac{A_i}{Max(A_i)} \quad (i \ for \ 40 \ and \ 50 \ Hz)$$

Consequently, each horizon has three attribute slices to demonstrate frequency responses.

5.3.1 BCU frequency responses

The low-frequency attribute slice shows several strong responses. Existing wells are located in these abnormal areas, such as the 2/7-19, 2/7-22, 2/7-29, and 2/7-31 wells (Figure 26). The Embla oil field was discovered by the 2/7-9 and 2/7-20 wells, even though these two wells are located in weak responses area, which was caused by poor seismic data quality due to gas interference. Although the 2/10-2 well is plotted on the edge of a strong response, the well is located on the up-thrown side of a normal fault (Figure 29). The 2/10-1 well reported a gas kick in Permian Rotliegendes sands, and it did not show any significant abnormal responses.
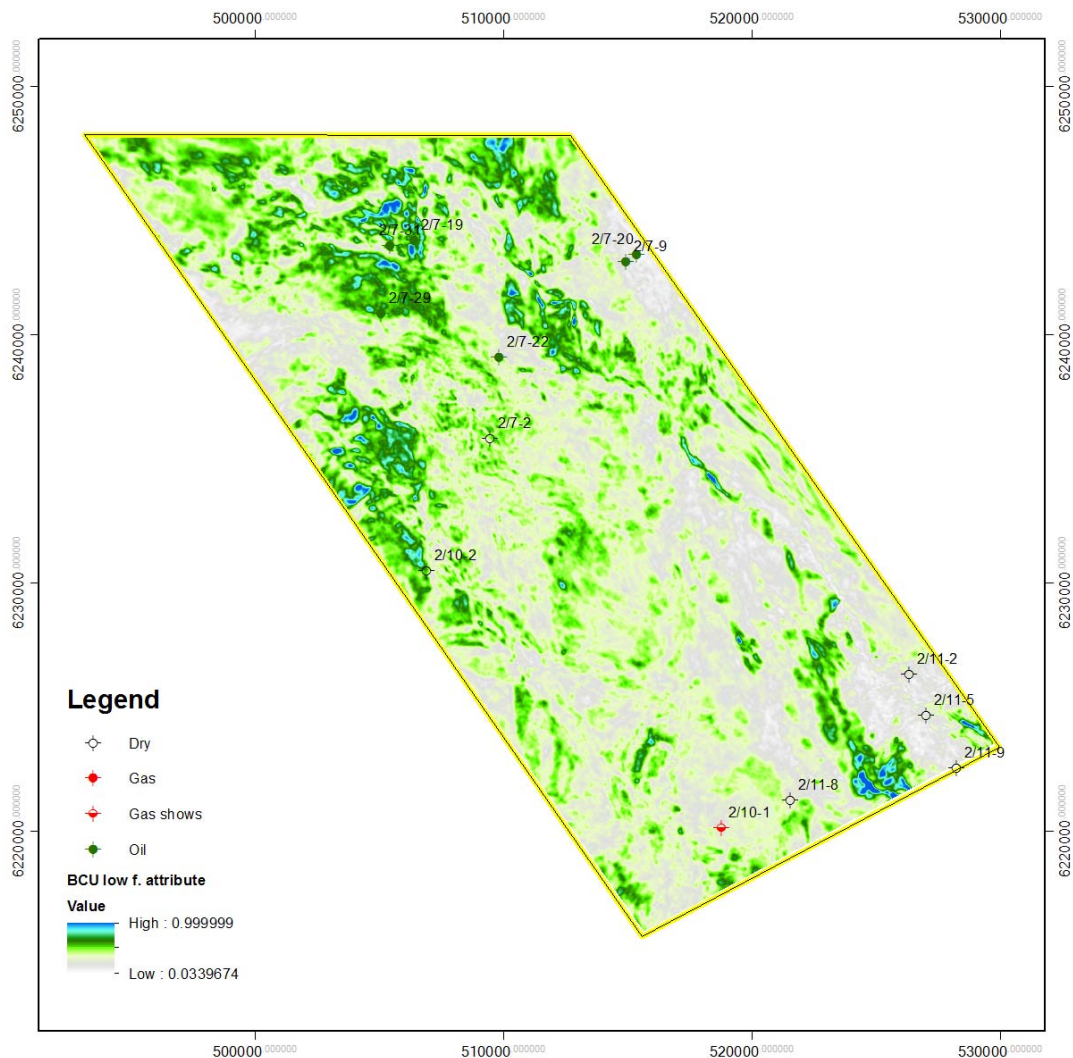

Figure 26. Low-frequency attribute within 200ms below BCU

The medium-frequency attribute slice shows similar responses with previous low-frequency attribute slice. But there are more pronounced anomalies present in the southern corner of seismic volume. In addition, the region west of the 2/10-2 well has the strongest responses (Figure 27).
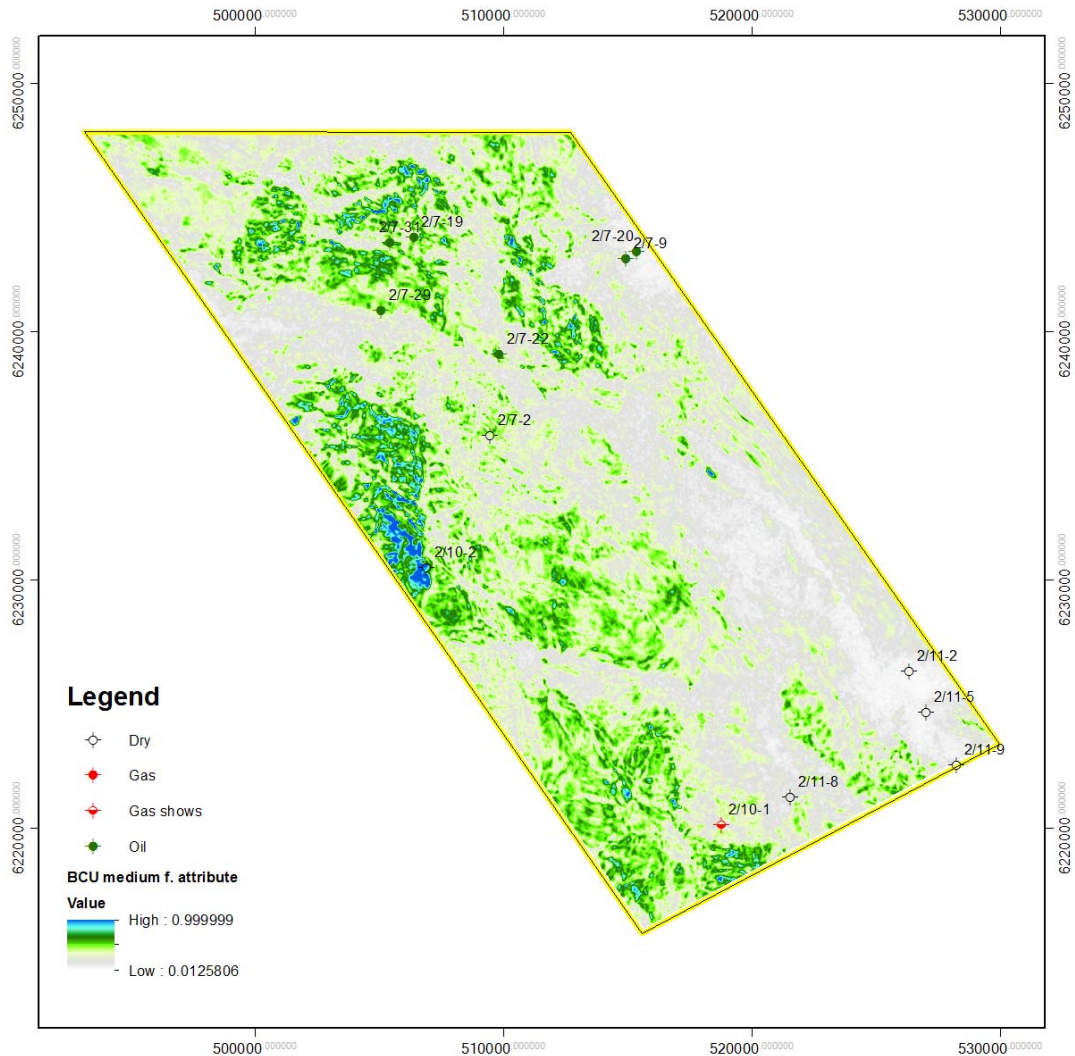

Figure 27. Medium-frequency attribute within 200ms below BCU

Frequency anomalies are weaker in the northern part of seismic volume in the high-frequency attribute slice (Figure 28), however, similar responses still remain in several areas, such as the east of the 2/7-22, west of the 2/7-2, and east of the 2/10-2,

which are considered to be favorable exploration prospects. The area between the 2-11-8 and 2/11-6 wells vanished completely.
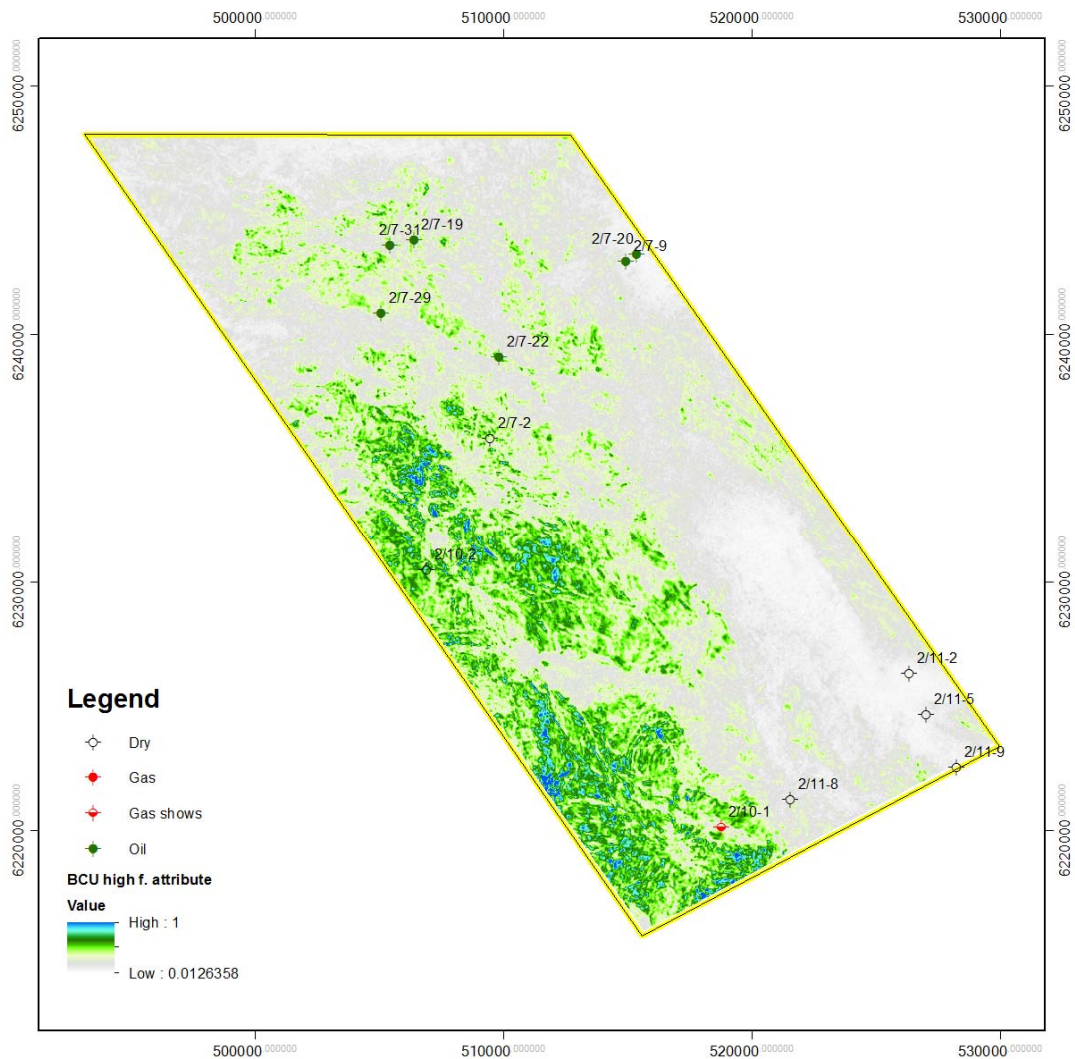

Figure 28. High-frequency attribute within 200ms below BCU

The low-frequency anomalies below the BCU (Figure 26) were plotted on the structural map of the overlying BCU. These anomalies distribute along the slope of the northern sub-sag or inside the depocenter of the southern sub-sag (Figure 29).

Upper Jurassic source rock, Kimmeridgian shale was deposited in the depocenter of the southern sub-sag. The low-frequency responses within this region might be directly produced by hydrocarbon generated from the hot shale.
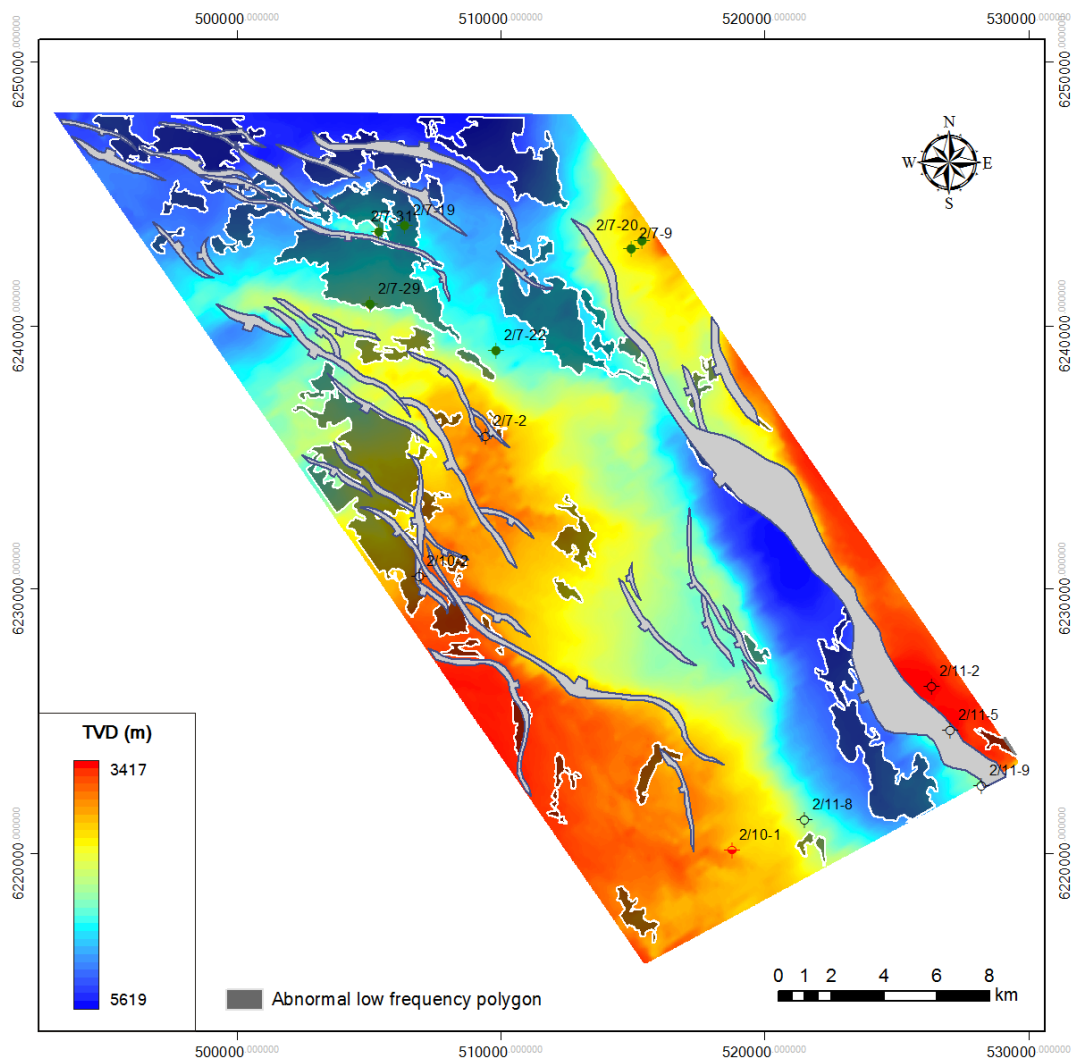
Figure 29. BCU structural map overlying low-frequency anomalies

(Faults are shown with grey polygons)

5.3.2 Late Cretaceous frequency responses

Although several wells encountered hydrocarbons in Upper Cretaceous chalk reservoirs, the low-frequency attribute slice does not show exciting coincidence between frequency responses and fluid content of wells (Figure 30). The 2/11-2 well from the Hod oilfield is located in seismic obscured area, and does not show abnormal responses. The same problem appears in both the 2/7-9 well located Embla field and

the Valhall field. Instead, on the rim of the Valhall and Hod fields, frequency attribute illustrates strong responses, which might be caused by residual oil around anticlines.

Furthermore, there is a widespread abnormal cloud to the west of the 2/7-2 well, and this location shows similar anomaly in the BCU frequency attribute slices.
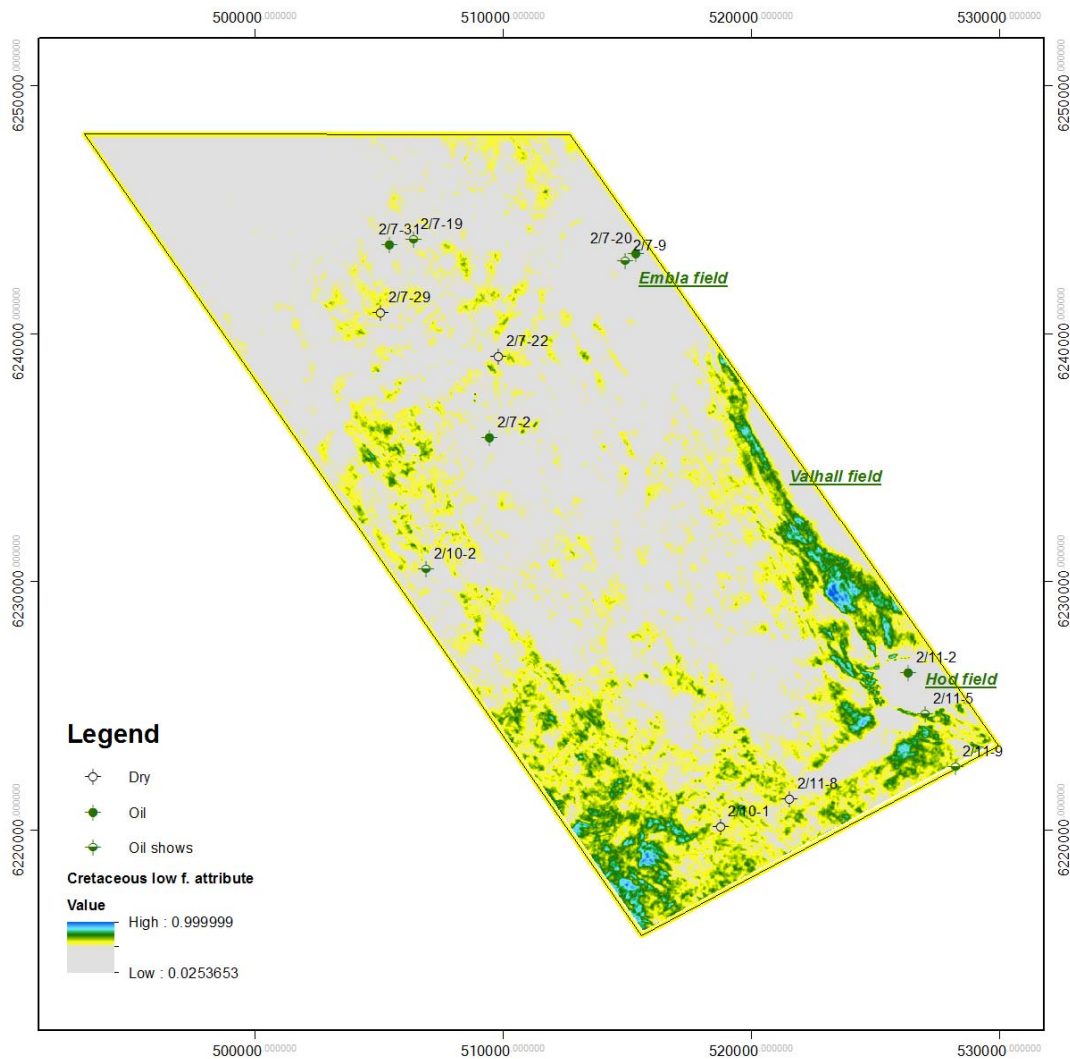

Figure 30. Low-frequency attribute within 200ms below Top Cretaceous

The medium-frequency attribute slice has inherited responses from the low-frequency responses (Figure 31). In comparison, the magnitude of the response to the west of the 2/7-2 well has been amplified, and instead, the responses surrounding existing oilfields have been weakened.
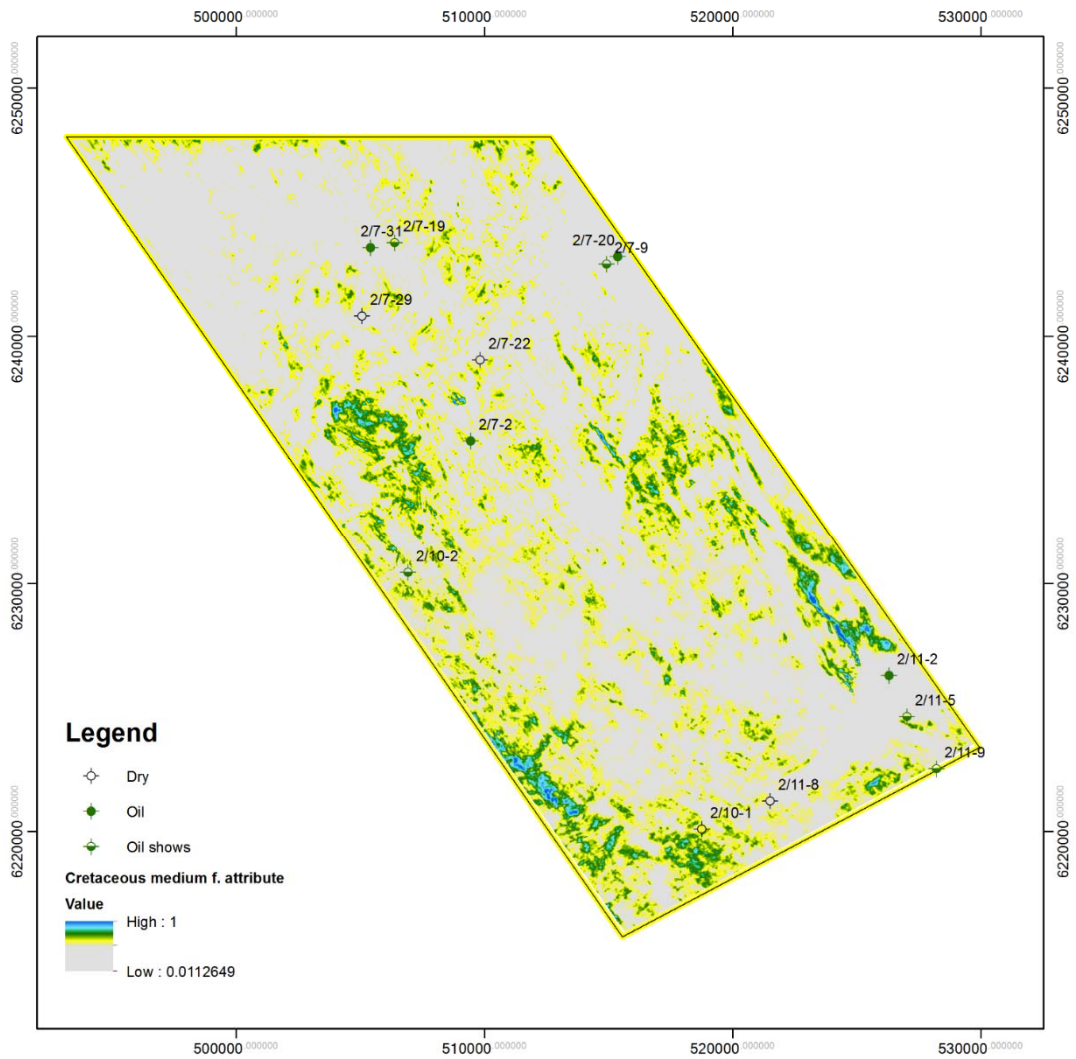
Figure 31. Medium-frequency attribute within 200ms below Top Cretaceous

The frequency responses on the rim of existing oilfields are eliminated on the high-frequency attribute slice, while the anomaly to the west of the 2/7-2 west still remains strong (Figure 32).

45
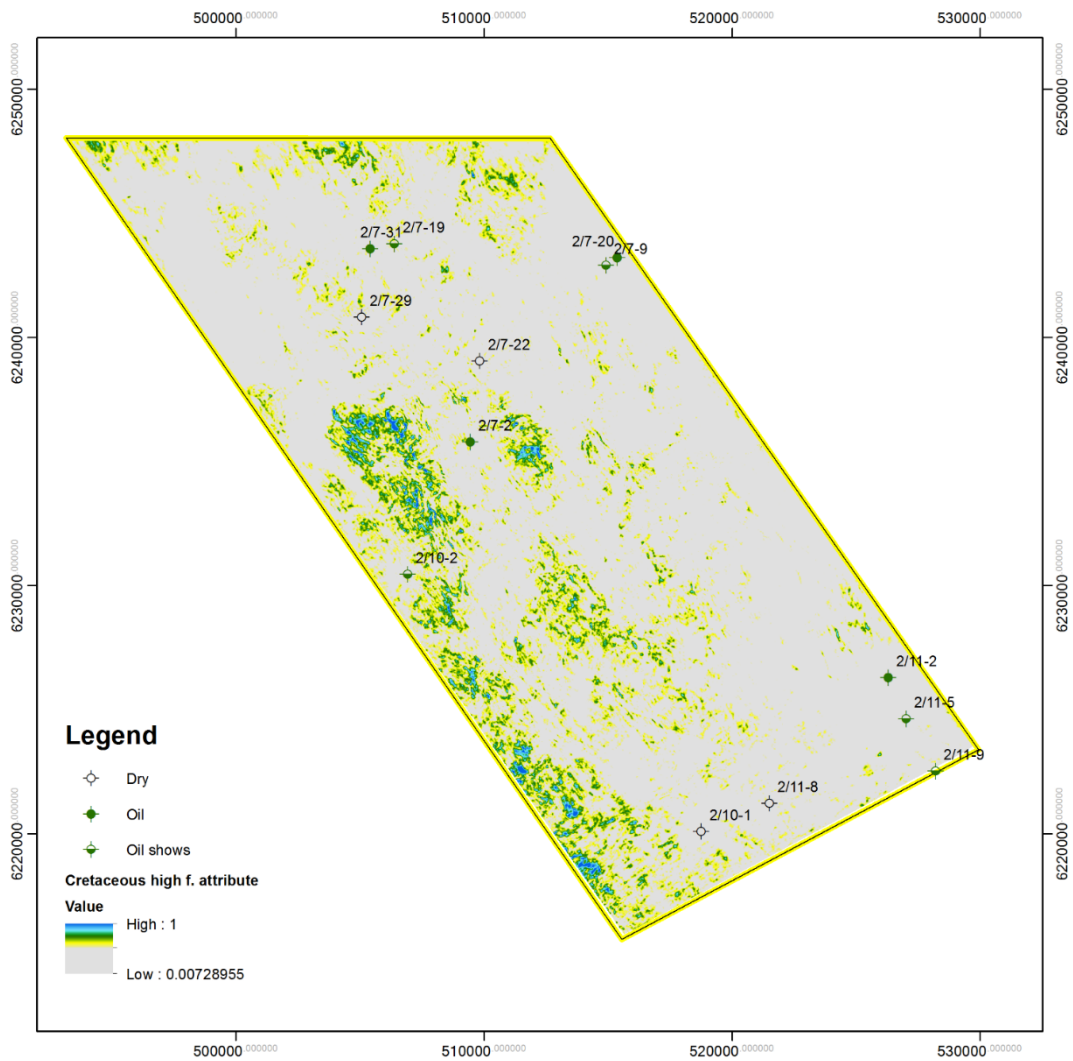
Figure 32. High-frequency attribute within 200ms below Top Cretaceous

Plotting the low-frequency anomalies below Top Cretaceous (Figure 30) onto the Top Cretaceous structural map, abnormal responses are seen distributed along the slope of the sub-sags or on the flank of Grensen Nose (Figure 33). The west of the 2/7-2 well and the western flank of the Lindesnes Ridge are regarded as favorable exploration targets for hydrocarbon saturated chalk reservoirs.

46
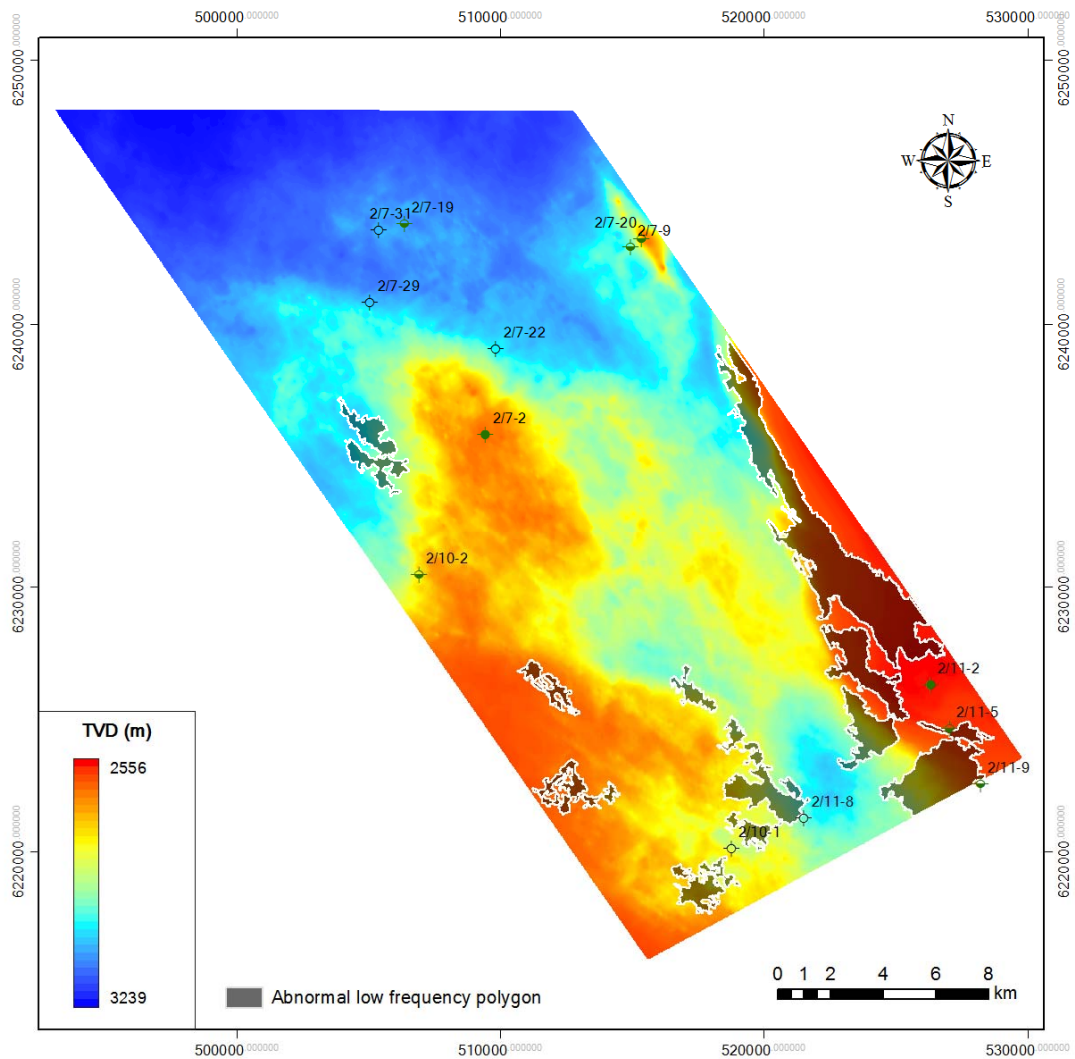
Figure 33. Top Cretaceous structural map overlying low-frequency anomalies

5.3.3 Late Paleogene frequency responses

In the shallow sections, hydrocarbons were discovered within Late Eocene clastic sands. The Hod oilfield displays strong frequency responses on the low-frequency attribute slice, and some sparkle anomalies appear in the Embla oilfield (Figure 34). The rest region is poor with frequency responses, which is corresponding to brine saturated reservoirs of penetrated wells.
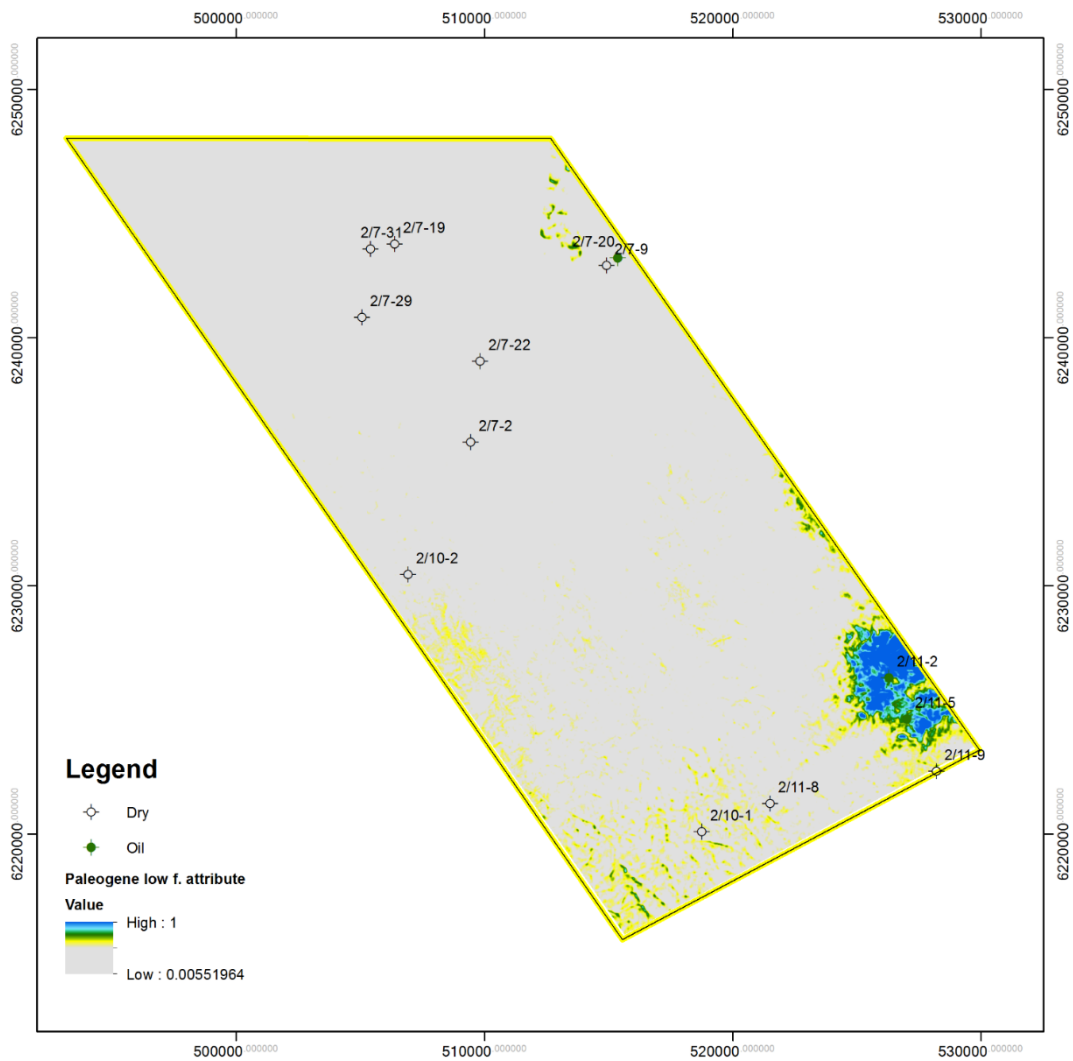
Figure 34. Low-frequency attribute within 180ms below Top Paleogene

The medium-frequency attribute slice shows slightly increasing area of anomalies, however, no significant area is expected for the purpose of petroleum exploration (Figure 35).
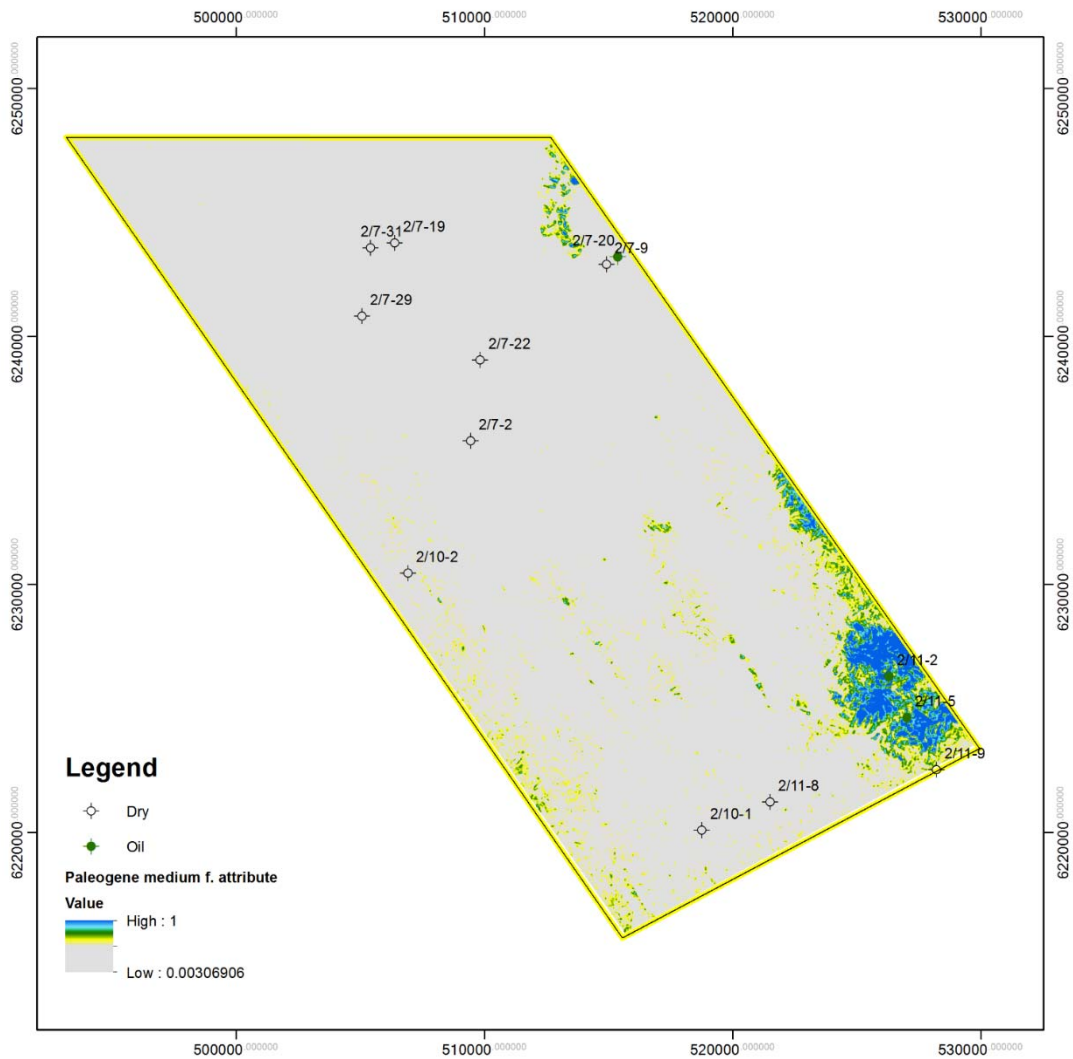
Figure 35. Medium-frequency attribute within 180ms below Top Paleogene

The high-frequency attribute slice (Figure 36) shows similar responses with the previous segments (Figure 34 and Figure 35). The magnitude from responses in the middle of Hod field is much lower than that from the rim, which can be explained by the hydrocarbons being concentrated within the uppermost cap of the anticlines, and high-frequency energy attenuated while penetrating through massive chalk reservoirs.

49
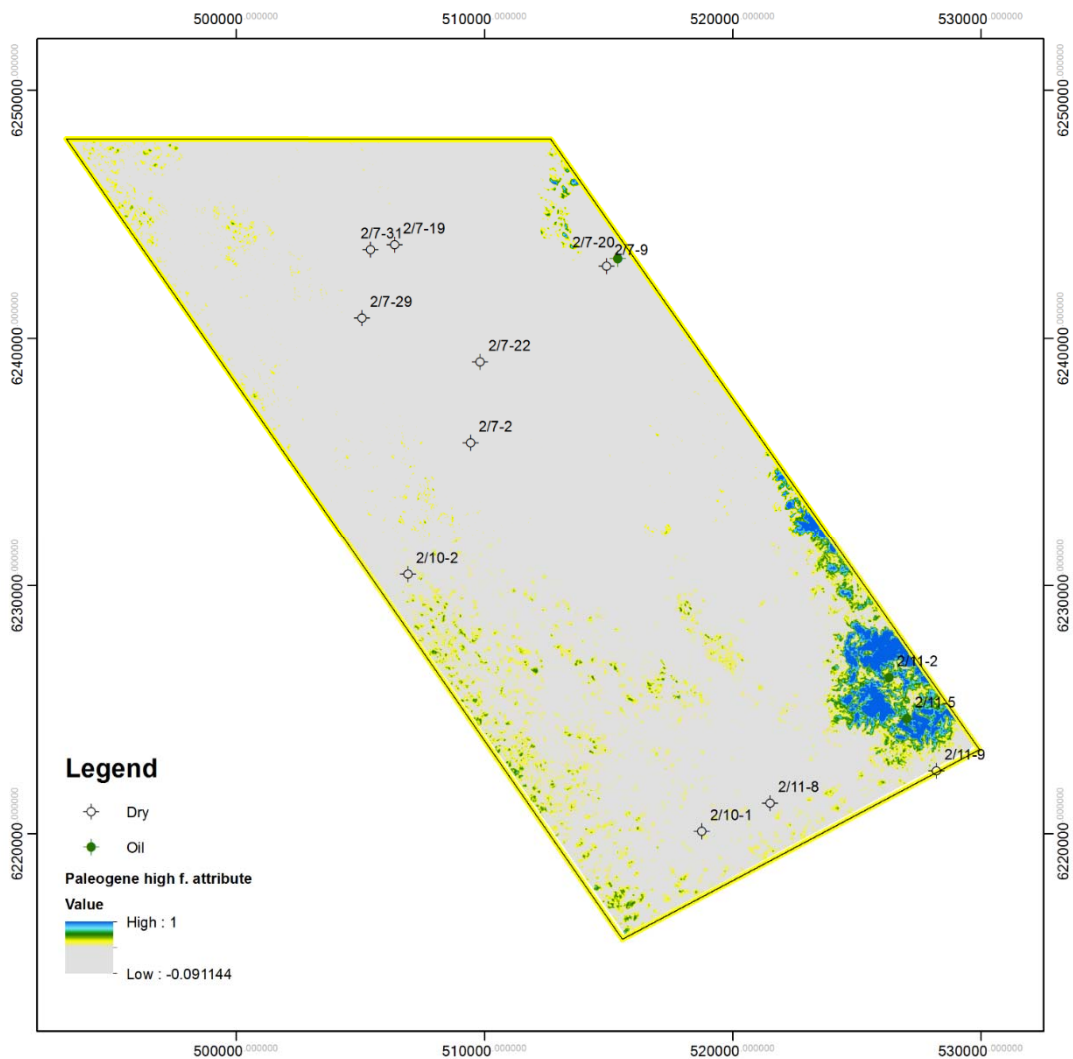
Figure 36. High-frequency attribute within 180ms below Top Paleogene

Plotting the low-frequency anomalies below Top Paleogene (Figure 34) onto the Top Paleogene structural map, anomalous response distribution is overlying the anticline (Figure 37). Considering no significant abnormal responses are characterized within the under-exploration area, no further prospects are recommended for the shallow sections.
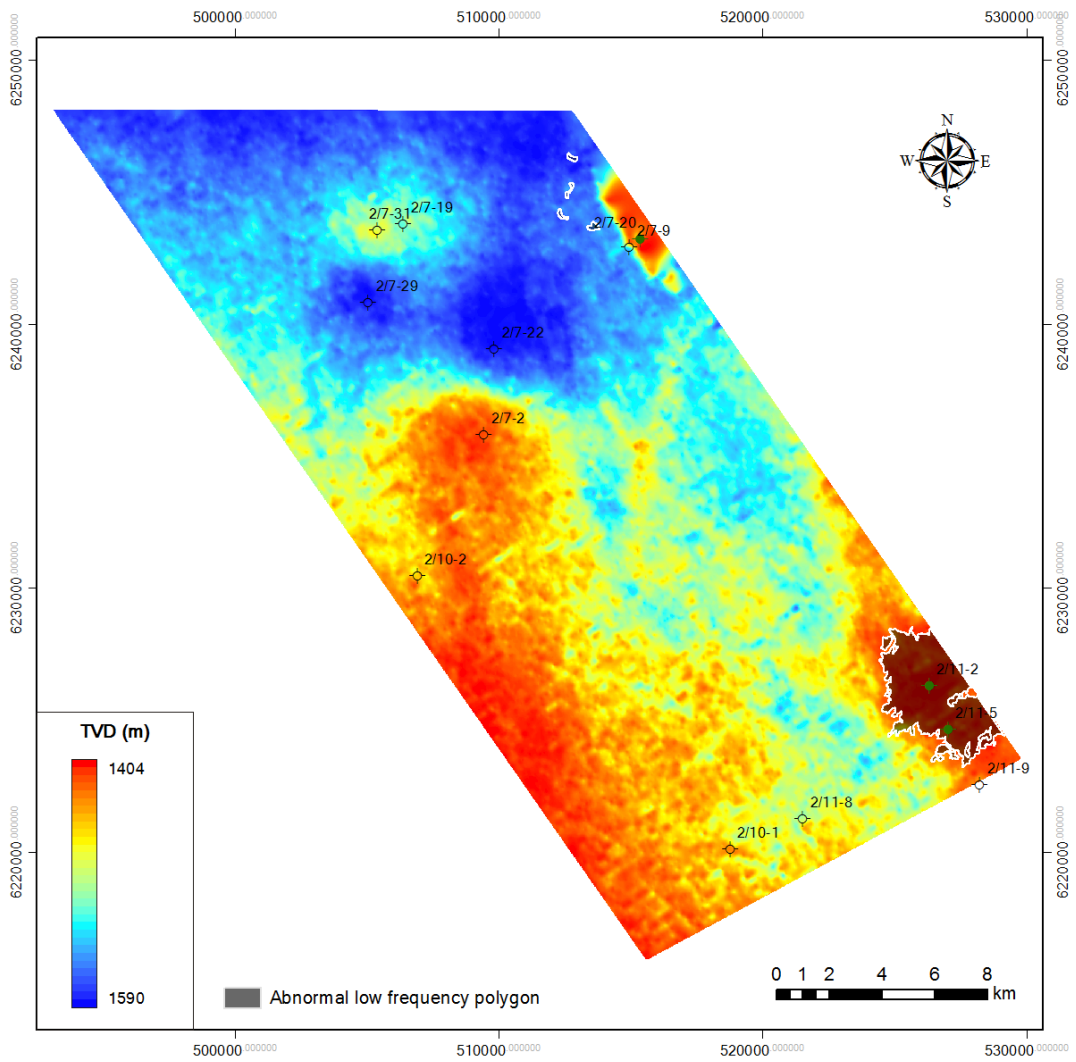
Figure 37. Top Paleogene structural map overlying low-frequency anomalies

5.4 Prospect identification

5.4.1 BCU prospects

The low-frequency seismic detected 96 km^2 of abnormal responses beneath the BCU. Responses within polygon C, D, F, and G are bounded by normal faults, while the rest, A, B, E, H, and I, are stratigraphy related (Figure 38).
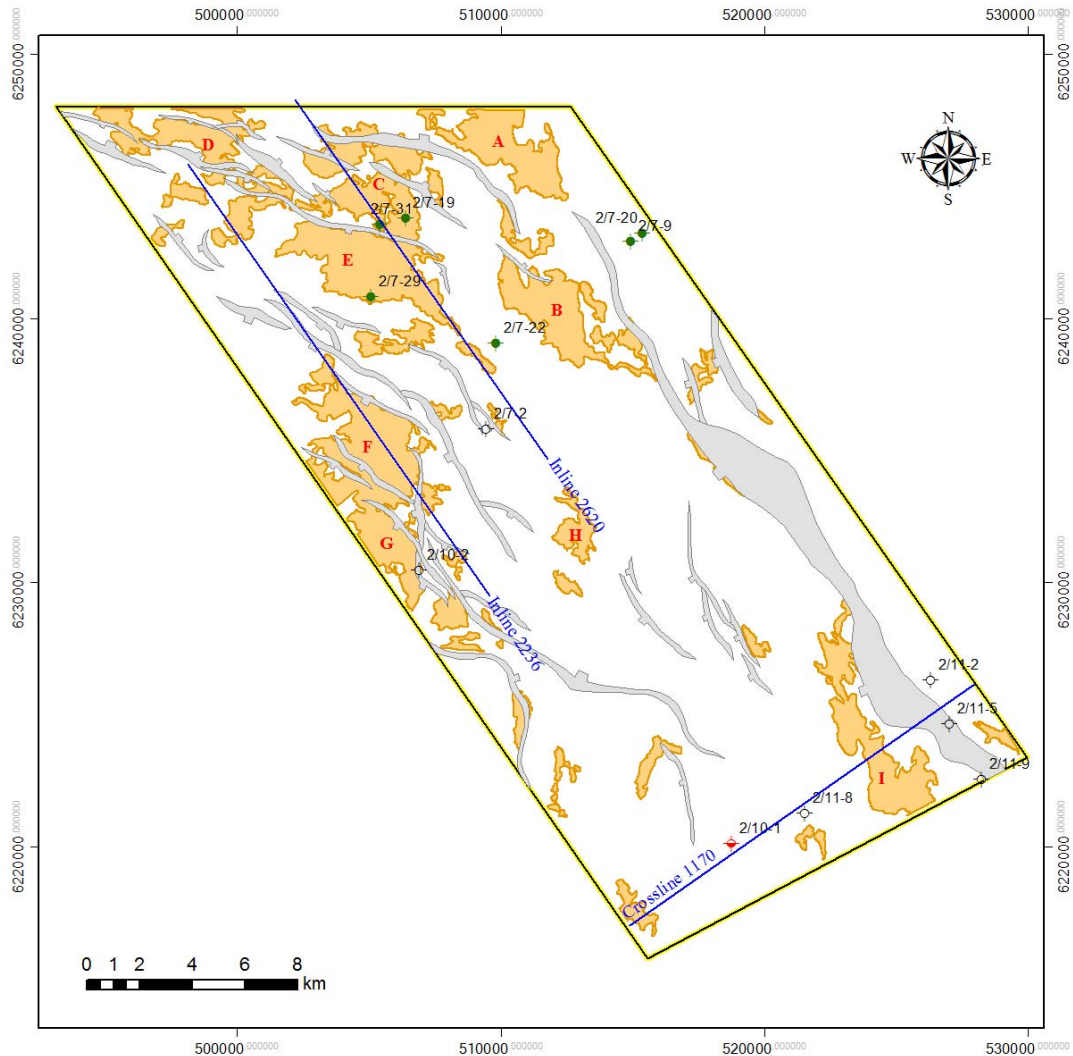
Figure 38. BCU clastic-reservoir polygons from low-frequency attribute slice

On conventional time-domain stacked seismic profiles, several bright spots with strong reflections beneath BCU indicate possible geo-bodies, which may comprise porous reservoirs. Such events are observed on frequency-domain seismic

sections crossing existing wells, e.g. the 2/7-29, 2/7-19, 2/7-22, and 2/7-31 wells, where hydrocarbons flowed from field tests. For instance, the 2/7-31 well penetrated a fault-bounded closure and tested hydrocarbon from Upper Jurassic Ula Sandstone, and strong frequency responses appear on the 10 Hz spectral section (Figure 39; line location see Figure 38 inline 2620). The downthrown side responses to the northwest direction have been tested by the 2/7-29 well, which obtained a one-gallon dead-oil sample in the Upper Jurassic Eldifisk Formation sandstone.
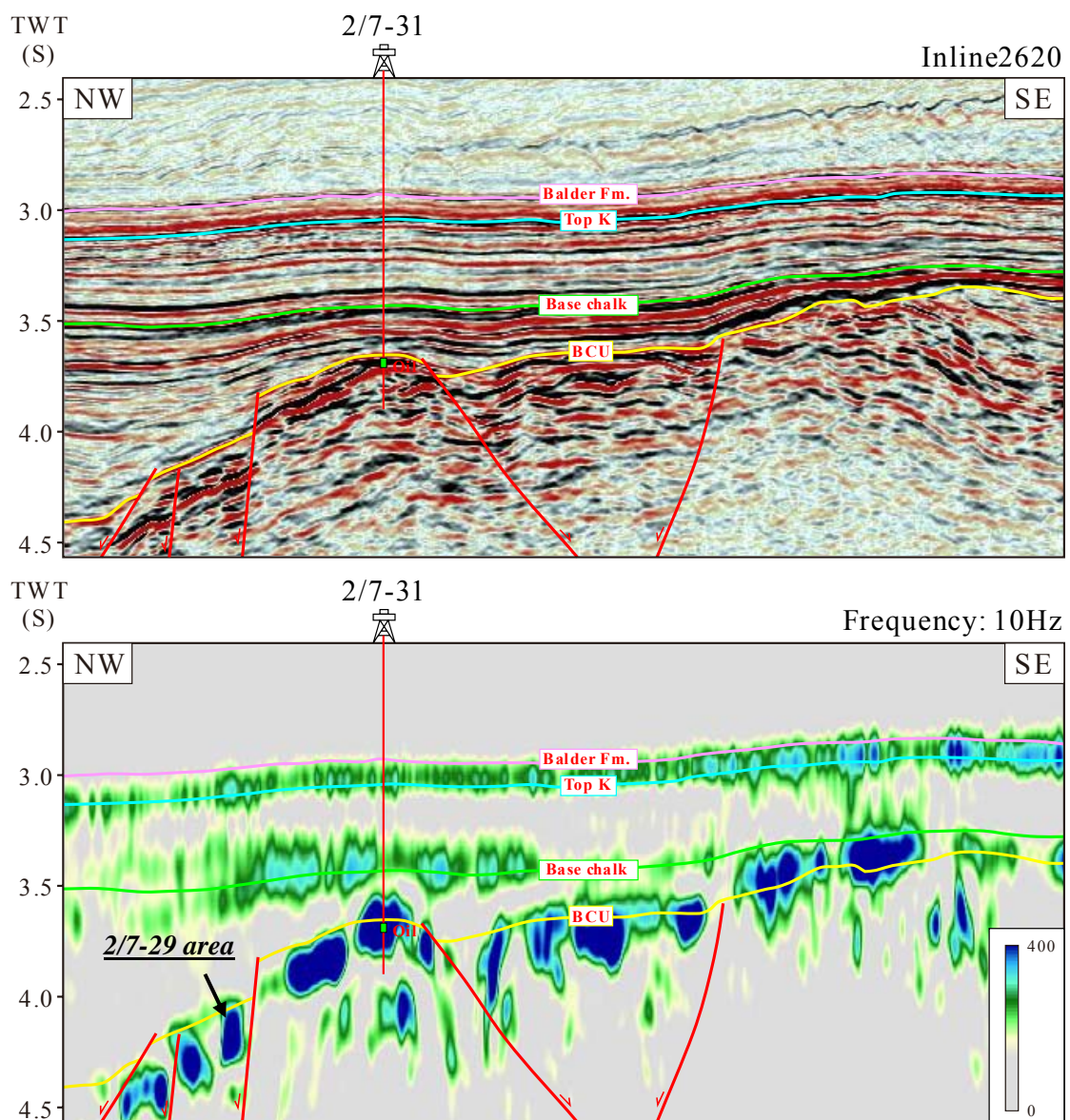
Figure 39. 10 Hz spectral section corresponding to the stacked seismic profile

On the flank of the Grensen Nose, there are several high-amplitude reflections on the stacked seismic, and strong responses are shown on the low-frequency envelope. These anomalies lie beneath the BCU, and possibly indicate the presence of hydrocarbons (Figure 40; line location see Figure 38 inline 2236). This type of reflection shows the same play concept with existing wells, e.g. the 2/7-31 well, which provides exciting evidence of hydrocarbon existence. Similar abnormal low-frequency spectra can be identified from polygon A, B, D, F, and G of the BCU prospect map (Figure 38), and the total coverage for these polygons is 43 km^2. The reservoir rock for these prospects is considered to be composed of sandstone from Upper Jurassic, Permian, or Devonian.
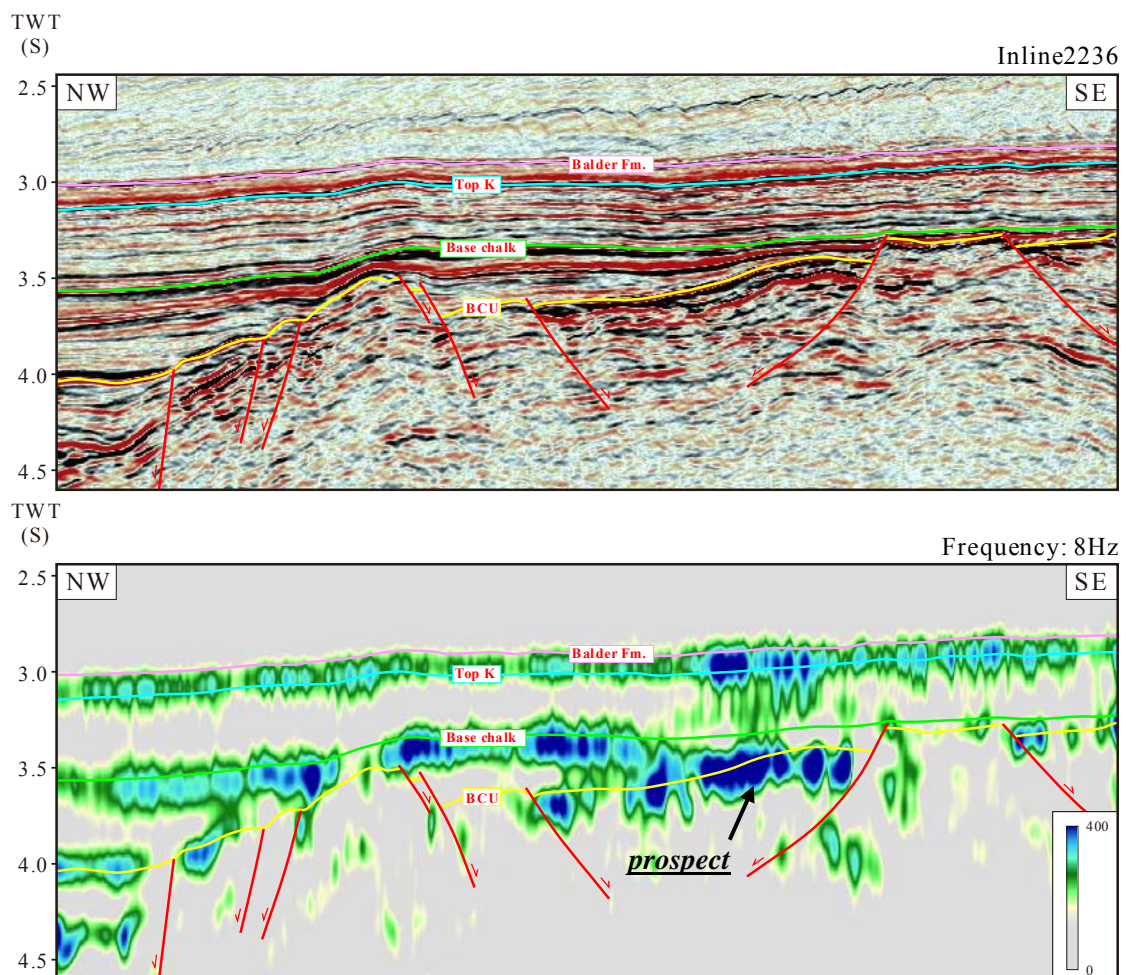
Figure 40. 8 Hz spectral section corresponding to the stacked seismic profile

In the depocenter of the southern sub-sag, strong low-frequency responses are observed on the 7.2 Hz spectral section (Figure 41; line location see Figure 38 crossline 1170). The anomaly might be produced by petroliferous reservoirs from low-stand-system-tract turbidite input along the valley, or it may have been triggered by oily shale of the Upper Jurassic source rock. The coverage of the polygon is near 10 km^2.
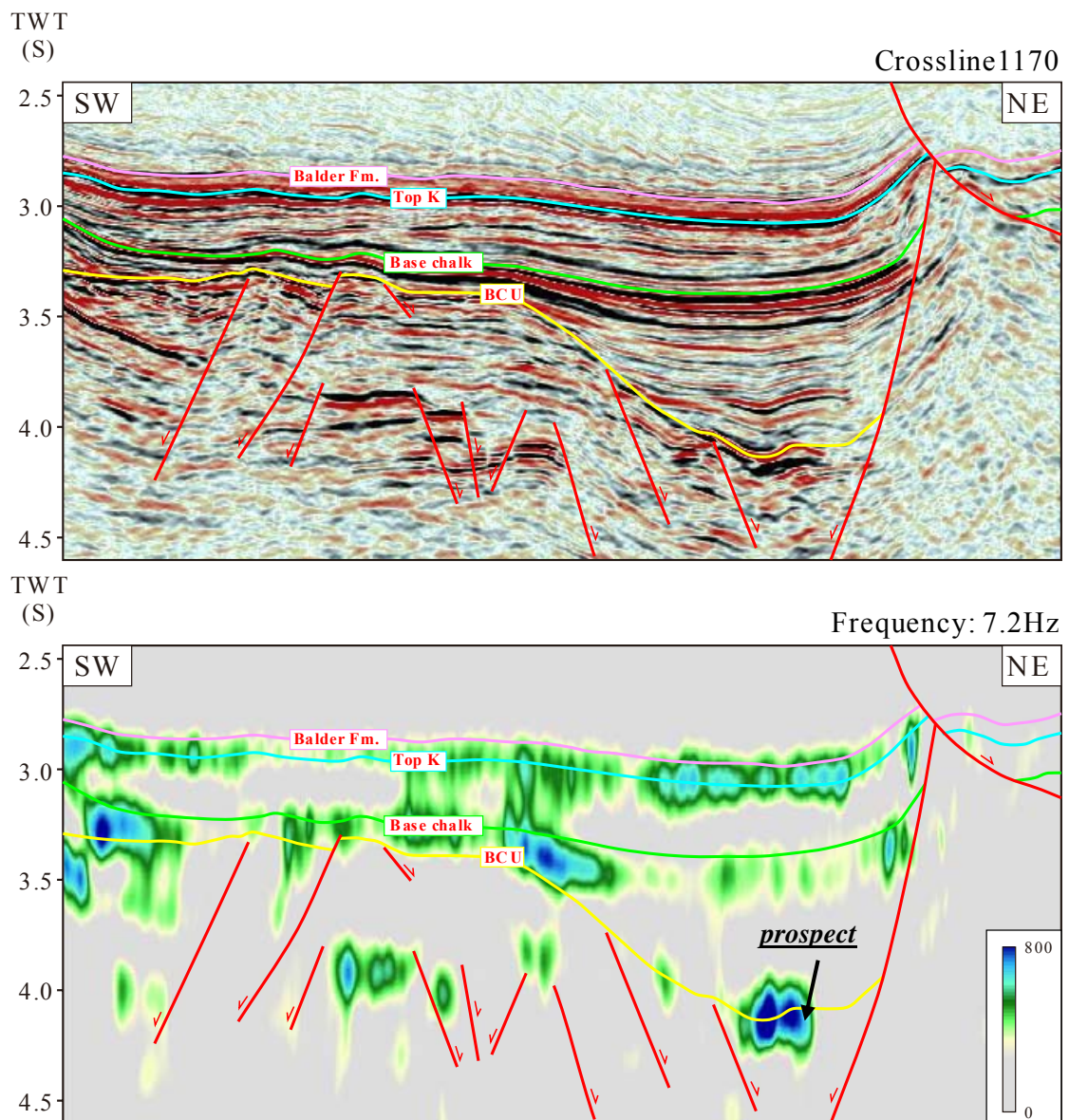
Figure 41. 7.2 Hz spectral section corresponding to the stacked seismic profile

5.4.2 Cretaceous prospects

The low-frequency seismic detected 43 km^2 of abnormal responses around the Top Cretaceous. Responses within polygon A, B, C, and D are associated with salt-induced anticlines on the Lindesnes Ridge (Figure 42). The polygon H area overlies the BCU prospect (polygon F and G on Figure 38), but the area is limited to 3 km^2.
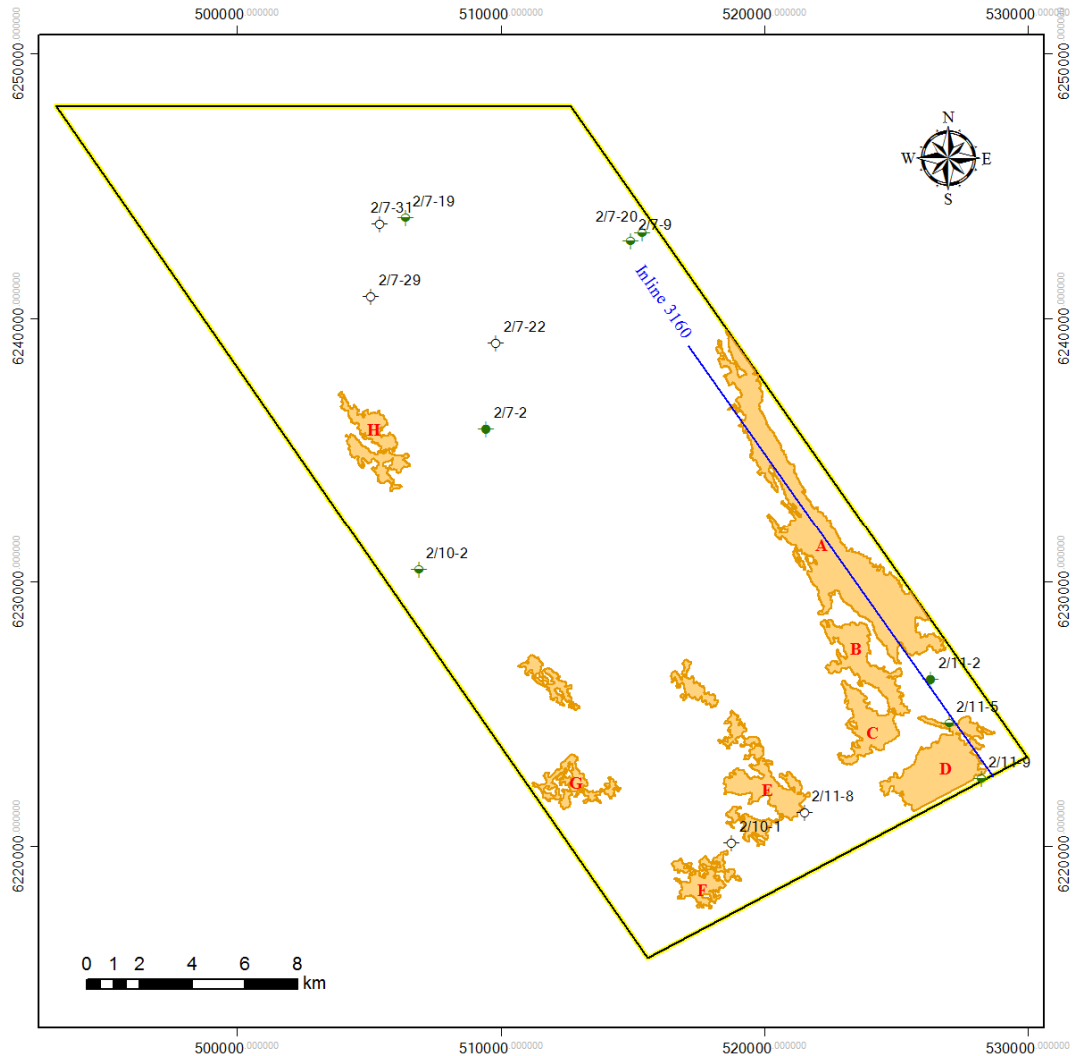
Figure 42. Cretaceous chalk reservoirs prospects from low-frequency seismic

On the western flank of the Lindesnes Ridge anticline, strong low-frequency responses are observed on the 12 Hz spectral section (Figure 43; line location see Figure 42 inline 3160). In the middle of the anticline for the chalk reservoirs, no

significant low-frequency responses were generated due to obscured seismic data. However, for the shallow section of Paleogene, hydrocarbon was proved by field tests. Tested hydrocarbons are associated with both high amplitude reflections from stacked seismic and strong responses from the low-frequency envelope.
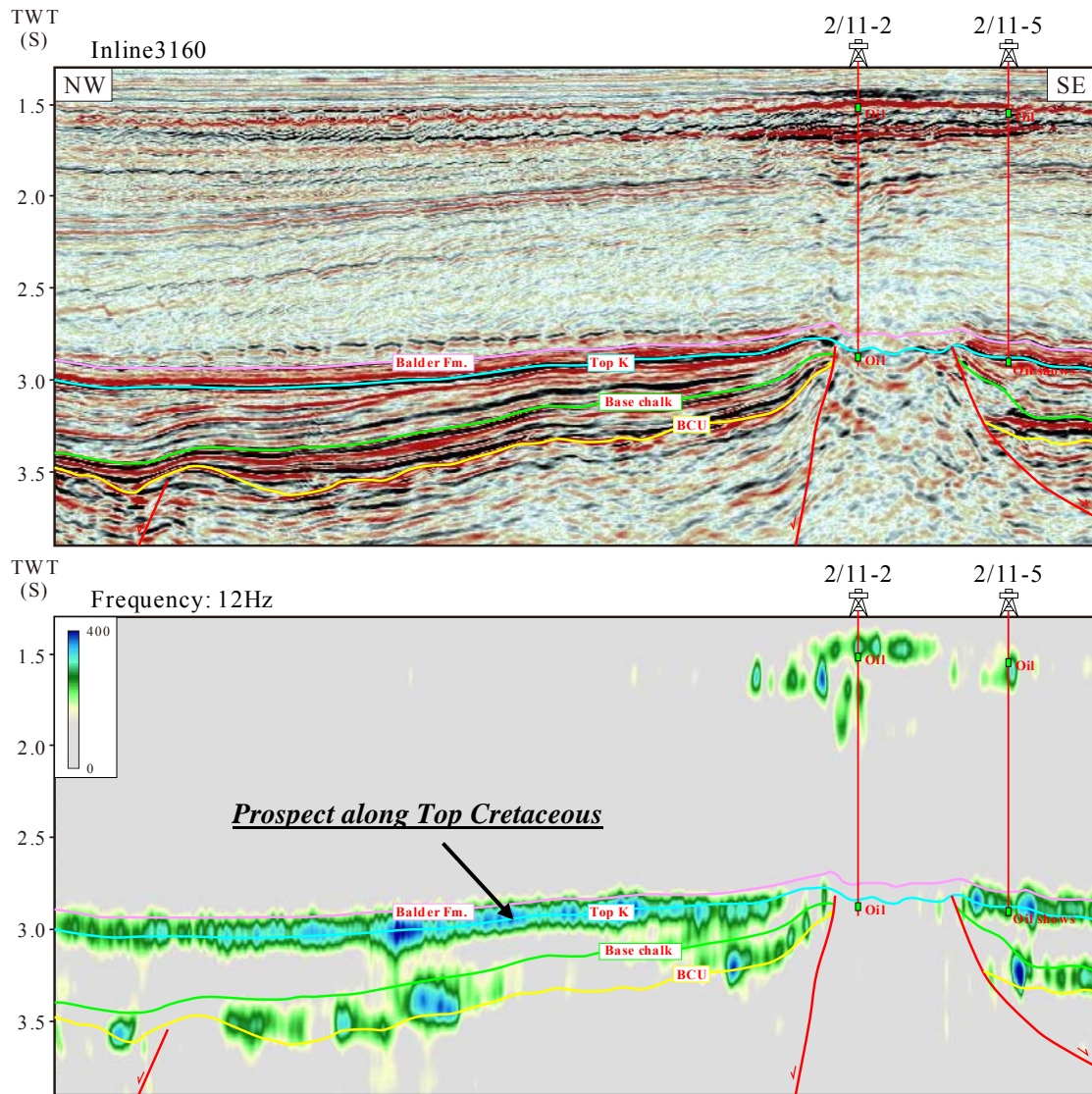
Figure 43. 12 Hz spectral section corresponding to the stacked seismic profile

6 Discussion

6.1 Slow wave interference

Slow waves can exist for all wavelengths when seismic wave propagate through porous media (Ferrazzini et al., 1987). The frequency-dependent loss mechanism is affected by P-wave attenuation from slow-wave diffusion. Variations of fluid saturation, permeability, and mineral properties in reservoirs can drastically alter the attenuation and velocity dispersion (Picotti et al., 2006).

As the result, anomalies of frequency responses appear on surfaces where stratigraphy varies abruptly, e.g. the Paleogene Balder Formation, Top Cretaceous, the base of Cretaceous chalk, the BCU, etc. (Figure 43). This explains why continuous frequency anomalies have been developed along critical horizons and some discontinuous frequency responses are distributed along fault planes.

Therefore, in addition to conventional stacked seismic, frequency spectral data can be applied to verify the interpretation of horizons and faults.

6.2 Magnitude of frequency attributes

Time-frequency envelopes are produced by transforming seismic from time-domain to frequency-domain, and the parameters of the algorithm affect the magnitudes of frequency attributes. After Gabor-Morlet transform, the maximum magnitude of frequency amplitude decreases from low- to high-frequency envelopes (see the color bars on Figure 20, Figure 21, Figure 22, Figure 23, Figure 24, and Figure 25).

For current spectral volumes, the maximum amplitude of 4 Hz envelope reached the magnitude of 4546, and decreased to 876 on the 20 Hz envelope, then declined to 248 on the 40 Hz cube. Accordingly, it is not easy to designate empirical thresholds of amplitude magnitude to highlight non-hydrocarbon related responses.

As a practical solution, petroliferous intervals from discovered wells should be utilized to determine the top of oil/gas interval, gas-water contact, and oil-water

58

contact. The thresholds can be ultimately read on corresponding projections of critical well tops, and then be plugged into color ramp initialization to produce spectral sections, which exhibit hydrocarbon-related characteristics.

6.3 Frequency responses on heterogeneous reservoirs

Since seismic amplitude loss is associated with variations of reservoir properties, heterogeneity at the reservoir-scale may be directly reflected from the frequency-dependent responses. Closures from structural mapping ordinarily have neat and smooth boundaries, whereas their geometries from frequency responses do not necessarily remain the same. On the maps of potential prospects (Figure 38 and Figure 42), polygons of prospects show indented edges which may be the result of heterogeneity of reservoirs and require further evidence from drilling wells.

7 Conclusion

Spectral data can be obtained by transforming seismic from time to frequency domain with spectral decomposition methods. Anomalous low-frequency seismic responses at frequency less than 20 Hz appear very often to hydrocarbon-saturated reservoirs and can be applied to determine fluid mobility. Penetrated wells show that low-frequency amplitude anomalies cover the entire section of pay zones. Instead, on higher frequency profiles, abnormal responses have been vanished inside pay zones, and appear either above or below the petroliferous intervals. This kind of low-frequency shadow effect is so called amplitude attenuation, which illustrates the vertical variation of fluid content and can be applied to detect hydrocarbons directly.

Beyond discovered fields, a total of 140 km^2 of prospects have been identified from the Cretaceous chalk reservoirs and sandstones beneath the BCU. The chalk prospects are distributed along the rim of anticlines surrounding the Lindesnes Ridge, whereas the BCU prospects are located on the slope of the Grensen Nose and had been stratigraphically entrapped.

Loss at higher seismic frequencies seems to be related to lithological variations. The heterogeneity of stratigraphy somehow produces abnormal responses on frequency envelopes. Besides their use for detecting hydrocarbons, spectral data can be applied to assist in monitoring horizons and faults during seismic interpretation.

References

Blystad, P., Brekke, H., Farseth, R. B., Larsen, B. T., Skogseid, J., & Torudbakken, B. (1995). Structural elements of the Norwegian continental shelf . Part II: The Norwegian Sea Region. Stavanger, Norwegian Petroleum Directorate.

Brasher, J. E., & Vagle, K. R. (1996). Influence of lithofacies and diagenesis on Norwegian North Sea chalk reservoirs. AAPG Bulletin, 80(5), 746-768.

Brekke, H. (2000). The tectonic evolution of the Norwegian Sea Continental Margin with emphasis on the Vøring and Møre Basins. In: Dynamics of the Norwegian Margin (Ed. by A. Nøttvedt, B. T. Larsen, B. Olaussen et al.), pp. 327-378. Geological Society of London, London.

Cai, H., He, Z., & Huang, D. (2008). Application of frequency information to the prediction of hydrocarbon potential in carbonate reef flat reservoirs. Lithologic Reservoirs, 20(4), 113-117.

Casey, B., Romani, R., & Schmitt, R. (1993). Appraisal geology of the Saltire Field, Witch Ground Graben, North Sea. Geological Society, London, Petroleum Geology Conference series, Geological Society of London.

Castagna, J. P., Sun, S., & Siegfried, R. W. (2003). Instantaneous spectral analysis: Detection of low-frequency shadows associated with hydrocarbons. The Leading Edge, 22(2), 120-127.

Castagna, J. P., & Sun, S. (2006). Comparison of spectral decomposition methods. First Break, 24(3).

Chakraborty, A., & Okaya, D. (1995). Frequency-time decomposition of seismic data using wavelet-based methods. Geophysics, 60(6), 1906-1916.

Chen, X., He, Z., Pei, X., Zhong, W., & Yang, W. (2013). Numerical simulation of frequency-dependent seismic response and gas reservoir delineation in turbidites: A case study from China. Journal of Applied Geophysics, 94, 22-30.

Chen, X. H., He, Z. H., Zhu, S. X., Liu, W., & Zhong, W. L. (2012). Seismic low-frequency-based calculation of reservoir fluid mobility and its applications. Applied Geophysics, 9(3), 326-332.

Deegan, C. E., & Scull, B. J. (1977). A standard lithostratigraphic nomenclature for the central and northern North Sea. London, Norwegian Petroleum Directorate.

Ferrazzini, V., & Aki, K. (1987). Slow waves trapped in a fluid-filled infinite crack: Implication for volcanic tremor. Journal of Geophysical Research: Solid Earth (1978–2012), 92(B9), 9215-9223.

Gautier, D. L. (2005). Kimmeridgian Shales Total Petroleum System of the North Sea Graben Province. U.S. Geological Survey Bulletin, 2204-C, 1-24.

Gennaro, M., Wonham, J. P., Gawthorpe, R., & Sælen, G. (2013). Seismic stratigraphy of the Chalk Group in the Norwegian Central Graben, North Sea. Marine and Petroleum Geology, 45(0), 236-266.

Goledowski, B., Nielsen, S. B., & Clausen, O. R. (2012). Patterns of Cenozoic sediment flux from western Scandinavia. Basin Research, 24(4), 377-400.

Goloshubin, G. M., Korneev, V. A., & Vingalov, V. M. (2002). Seismic low-frequency effects from oil-saturated reservoir zones. 2002 SEG Annual Meeting,

Herrington, P. M., Pederstad, K., & Dickson, J. A. D. (1991). Sedimentology and diagenesis of resedimented and rhythmically bedded chalks from the Eldfisk Field, North Sea Central Graben. AAPG Bulletin, 75(11), 1661-1674.

Huang, Z., Wang, Y., Sun, X., & Wang, G. (2007). The gas reservoir response in PP- and PS-wave frequency sections. Applied Geophysics, 4(1), 51-57.

Jenyon, M. K. (1985). Basin-edge diapirism and updip salt flow in zechstein of southern North Sea. AAPG Bulletin, 69(1), 53-64.

Kazemeini, S. H., Juhlin, C., Zinck-Jørgensen, K., & Norden, B. (2009). Application of the continuous wavelet transform on seismic data for mapping of channel deposits and gas detection at the CO_2 sink site, Ketzin, Germany. Geophysical Prospecting, 57(1), 111-123.

Knight, I. A., Allen, L. R., Coipel, J., Jacobs, L., & Scanlan, M. J. (1993). The Embla Field. Petroleum Geology Conference series. 4: 1433.

Lee, M., & Hwang, Y. (1993). Tectonic evolution and structural styles of the East Shetland Basin. Geological Society, London, Petroleum Geology Conference series, Geological Society of London.

Liu, L., Cao, S., Li, X., Wang, L., Jiang, S., Chen, B., & Wang, X. (2010). Low-frequency seismic response characteristics of unconsolidated gas-bearing reservoirs. Oil Geophysical Prospecting, 45(6), 873-878.

Long, F., Chen, X., & He, Z. (2012). Numerical simulation of low-frequency amplitude anomaly in reservois and its application. Xinjiang Petroleum Geology, 33(1), 95-97.

Müller, B., Zoback, M. L., Fuchs, K., Mastin, L., Gregersen, S., Pavoni, N., Stephansson, O., & Ljunggren, C. (1992). Regional patterns of tectonic stress in Europe. Journal of Geophysical Research: Solid Earth, 97(B8), 11783-11803.

Maliva, R. G., & Dickson, J. A. D. (1992). Microfacies and diagenetic controls of porosity in Cretaceous/Tertiary chalks, Eldfisk field, Norwegian North Sea. AAPG Bulletin, 76(11), 1825-1838.

Mallat, S. G., & Zhang, Z. (1993). Matching pursuits with time-frequency dictionaries. Signal Processing, IEEE Transactions on, 41(12), 3397-3415.

Marshall, J., & Hewett, T. (2003). Devonian. In: The Millennium Atlas: Petroleum Geology of the central and northern North Sea (Ed. by D. Evans, C. Graham, A. Armour and P. Bathurst), pp. 65-81. Geological Society of London, London.

Morlet, J., Arens, G., Fourgeau, E., & Glard, D. (1982). Wave propagation and sampling theory-Part II: Complex signal and scattering in multilayered media. Geophysics, 47(2), 203-221.

Mosar, J. (2003). Scandinavia's North Atlantic passive margin. Journal of Geophysical Research: Solid Earth, 108(B8), 2360.

Munz, I. a., Iden, K., Johansen, H., & Vagle, K. (1998). The fluid regime during fracturing of the Embla field, Central Trough, North Sea. Marine and Petroleum Geology, 15(8), 751-768.

NPD (2014). Factpages. 2014, from http://www.npd.no. Seen on 26 March 2014.

Odebeatu, E., Zhang, J., Chapman, M., Liu, E., & Li, X. (2006). Application of spectral decomposition to detection of dispersion anomalies associated with gas saturation. The Leading Edge, 25(2), 206-210.

Ohm, S. E., Karlsen, D. A., Phan, N. T., Strand, T., & Iversen, G. (2012). Present Jurassic petroleum charge facing Paleozoic biodegraded oil: Geochemical challenges and potential upsides, Embla field, North Sea. AAPG Bulletin, 96(8), 1523-1552.

Okaya, D. A., Karageorgi, E., McEvilly, T. V., & Malin, P. E. (1992). Removing vibrator-induced correlation artifacts by filtering in frequency-uncorrelated time space. Geophysics, 57(7), 916-926.

Pang, R., Liu, B., & sun, C. (2013). Review on time-frequency analysis technique and its application in seismic exploration. Lithologic Reservoirs, 25(3), 92-101.

Partyka, G., Gridley, J., & Lopez, J. (1999). Interpretational applications of spectral decomposition in reservoir characterization. Leading Edge (Tulsa, OK), 18(3).

Picotti, S., Carcione, J. M., & Picotti, S. (2006). P-wave seismic attenuation by slow-wave diffusion: Effects of inhomogeneous rock properties. Geophysics, 71(3), 11-21.

Pu, Y. (2011). Multiple seismic indentification technologies application in deep reef reservoir in Yuanba area. Natural Gas Industry, 31(10), 27-31.

Qian, S., & Chen, D. (1994). Signal representation using adaptive normalized Gaussian functions. Signal processing, 36(1), 1-11.

Qian, S., & Chen, D. (1999). Joint time-frequency analysis. Signal Processing Magazine, IEEE, 16(2), 52-67.

Rawson, P. F., & Riley, L. A. (1982). Latest Jurassic-Early Cretaceous events and the "late Cimmerian unconformity" in North Sea area. AAPG Bulletin, 66(12), 2628-2648.

Rossland, A., Escalona, A., & Rolfsen, R. (2013). Permian-hobcene tectonostratigraphic evolution of the Mandal high, central graben, North Sea. AAPG Bulletin, 97(6), 923-957.

Silin, D., & Goloshubin, G. (2010). An asymptotic model of seismic reflection from a permeable layer. Transport in porous media, 83(1), 233-256.

Sinha, S., Routh, P. S., Anno, P. D., & Castagna, J. P. (2005). Spectral decomposition of seismic data with continuous-wavelet transform. Geophysics, 70(6), 19-25.

Stockwell, R., Manshinha, L., & Lowe, R. (1996). Localization of the complex spectrum: The S-transform. IEEE Transactions on: Signal Processing. 44(4), 998-1001.

Sun, S., Castagna, J. P., & Siegfried, R. (2002). Examples of enhanced spectral processing in direct hydrocarbon detection. 72nd Annual Meeting, Society of Exploration Geophysicists. Expanded Abstracts,

Surlyk, F., Dons, T., Clausen, C. K., & Higham, J. (2003). Upper Cretaceous. In: The Millennium Atlas: Petroleum Geology of the central and northern North Sea (Ed. by D. Evans, C. Graham, A. Armour and P. Bathurst), pp. 213-233. Geological Society of London, London.

Taner, M. (1983). Joint Time/Frequency Analysis, Q Quality Factor and Dispersion Computation Using Gabor-Morlet Wavelets or the Gabor-Morlet Transform. Rock Solid Images internal report, RSI Technical Report.

Taner, M. T., Koehler, F., & Sheriff, R. (1979). Complex seismic trace analysis. Geophysics, 44(6), 1041-1063.

Taylor, M., Dillon, W., & Pecher, I. (2000). Trapping and migration of methane associated with the gas hydrate stability zone at the Blake Ridge Diapir: new insights from seismic data. Marine Geology, 164(1), 79-89.

Wang, D., He, Z., & Huang, D. (2009). Time-frequency spectral analysis application in petroliferous reservoir prediction. Natural Gas Industry, 29(4), 1-3.

Wilson, R. W., McCaffrey, K. J. W., Holdsworth, R. E., Imber, J., Jones, R. R., Welbon, A. I. F., & Roberts, D. (2006). Complex fault patterns, transtension and structural segmentation of the Lofoten Ridge, Norwegian margin: Using digital mapping to link onshore and offshore geology. Tectonics, 25(4), TC4018.

Yang, L., He, Z., Wen, X., Yang, X., & Sheng, Q. (2012). Application of frequency attenuation attributes to oil and gas exploration in deep carbonate rocks. LITHOLOGIC RESERVOIRS, 24(5), 98-101.

Yu, B. L., Zhou, L. P., & Wang, X. H. (2011). Application of the oil-bearing prediction methods based on spectral decomposition. SPG/SEG Shenzhen 2011 International Geophysical Conference. Shenzhen: 92-98.

Zanella, E., & Coward, M. P. (2003). Structural framework. In: The Millennium Atlas: Petroleum Geology of the central and northern North Sea (Ed. by D. Evans, C. Graham, A. Armour and P. Bathurst), pp. 45-59. Geological Society of London, London.

Zhang, D. J., Zou, W., Tao, Z. X., & Zhang, Y. (2012). Fluid identification based on Short-Time fractional Fourier Transform and its application. SEG Las Vegas 2012 Annual Meeting. SEG. Las Vegas 1-5.